2018-12-13

Characterizing Supercritical Methane Adsorption on Shale by a Multi-site Model

Wu, Zhe

UNIVERSITY OF CALGARY

CHARACTERIZING SUPERCRITICAL METHANE ADSORPTION ON SHALE BY A MULTI-SITE MODEL

by

Zhe Wu

A THESIS

SUBMITTED TO THE FACULTY OF GRADUATE STUDIES

IN PARTIAL FULFILMENT OF THE REQUIREMENTS FOR THE

DEGREE OF MASTER OF SCIENCE

GRADUATE PROGRAM IN CHEMICAL AND PETROLEUM ENGINEERING

CALGARY, ALBERTA

DECEMBER, 2018

Abstract

Shale gas, mainly consisting of adsorbed gas and free gas, has served a critical role of supplying the growing global natural gas demand in the past decades. Considering that the adsorbed methane has contributed up to 80% of the total gas in place (GIP), understanding the methane adsorption behaviors is imperative to an accurate estimation of total GIP. Historically, the single-site Langmuir-Gibbs model, with the assumption of a homogeneous surface, is commonly applied to estimate the adsorbed gas amount. However, this assumption cannot depict the methane adsorption characteristics due to various compositions and pore sizes of shales. In this work, a multi-site model integrating the energetic heterogeneity in adsorption is derived, which is also successfully validated with a series of measured adsorption isotherms in experimental conditions. Applying the proposed multi-site model for estimating GIP in shales can achieve more accurate results compared with using the traditionally single-site model. Furthermore, shale reservoir properties, such as reservoir porosity, a geothermal gradient, as well as a pressure gradient have been investigated and shown to affect the GIP.

Acknowledgements

Firstly, I want to express my sincere appreciation to my supervisor, Dr. Zhangxing (John) Chen, for this precious research opportunity he provides as well as his generous guidance and support during my research and studies at University of Calgary. His keen perspectives on research topics and positive attitudes towards life would continue to impress and inspire me.

Secondly, I am very grateful to my mentor, Dr. Zhaowen Li, for encouraging and motivating me to pursue a master's degree. He has shown the possibilities of graduate education and the perks of lifelong learning to me and many others by being an excellent role model in industry.

Thirdly, I am much obliged to our post-doctoral fellow, Dr. Jing Li, for the substantial time and energy he puts into assisting me with the creation of this work. Without his insightful knowledge of this research topic and timely support, I would not have completed this work at all.

Additionally, I would like to show my genuine gratitude to Dr. Jalel Azaiez and Dr. Roberto Aguilera for their time serving as my thesis defenses committee as well as their valuable suggestion and feedback for this thesis.

Finally, I would also like to thank all the staff members and students in our amazing research group Reservoir Simulation Group for making my academic journey here (2017-2018) a memorable one!

Dedication

To my family,

for their care, patience, and love

in all stages of my life.

Table of Contents

List of Tables

List of Figures and Illustrations

List of Symbols, Abbreviations and Nomenclature

Symbol	Definition
a	Parameter of RK-EOS method
b	Parameter of RK-EOS method
C	BET constant
D	Distance between nanopore walls, nm
E_a	Energy required to start the adsorption process, KJ/mol
E_d	Energy required to start the desorption process, KJ/mol
H	Reservoir depth, in km
ΔH	Differential enthalpy of adsorption, KJ/mol
I_H	Hydrogen index
I_o	Oxygen index
K	Henry's constant
M	Molar mass of methane, g/mol
n	Number of the adsorption sites that are available
n_T	Total gas amount, mol/g
n_a	Adsorbed gas amount, mol/g
n_{ab}	Absolute adsorption amount, mol/g
n_b	Bulk gas amount, mol/g
n_{ex}	Excess adsorption amount, mol/g
n_f	Amount of methane in the free gas phase, mol/g
n_{max}	Maximum adsorption capacity, mol/g
P	Equilibrium pressure for adsorption, MPa
P_c	Critical pressure of methane, MPa
P_0	Saturation pressure of adsorbates at the temperature of adsorption, MPa
P^0	Pressure at the perfect gas reference state, 0.1 MPa
P_0	Surface pressure, 0.1 MPa
P_H	Pressure at a specific reservoir depth, in MPa
$P_{L(i)}$	Langmuir pressure for the single adsorption site, MPa
P_L	Langmuir pressure, MPa
Q_m	Mean value for the adsorption heat of the adsorbent, KJ/mol
$Q_{st(i)}$	Adsorption heat for a single adsorption site, KJ/mol
S1	Amount of free hydrocarbon
S2	Number of hydrocarbons generated from thermal cracking
S3	Amount of carbon dioxide released
S_a^0	Entropy of the adsorbate of the adsorbed phase at the state when the adsorbent's surface is fully covered by the adsorbate, J/mol/K

S_g^0	Entropy of the adsorbate of the bulk phase at the atmospheric pressure, J/mol/K
$\Delta S_{(i)}^0$	Standard entropy for the single adsorption site, J/mol/K
ΔS^0	Standard molar integral entropy at saturation where the surface energy coverage approaches unity, J/mol/K
ΔS_m^0	Average or apparent standard entropy for adsorption, J/mol/k
T_{max}	Temperature for the maximum release of hydrocarbon
T_c	Critical temperature of methane, K
T_0	Surface temperature, 20 ^{0} C
T_H	Temperature at a specific reservoir depth, in ^{0} C
T_b	Boiling temperature of methane, 111.66 K
V	Molar volume of methane, cm^3/mol
V_T	Total volume of the measurement system, cm3/g
V_a	Volume of the adsorbed phase, cm^3/g
V_m	Volume of the monolayer adsorption amount, cm^3/g
V_t	Volume of the effective space and adsorbed phase volume, cm^3/g
V	Volume of the adsorption amount, cm^3/g
Z	Compressibility factor of methane in gas phase
α	Geothermal gradient, 2.83 ^{0} C/100 m
$\alpha_{(i)}$	Fraction of the single adsorption site
β	Pressure coefficient, 1.45 MPa/100 m
λ	Thermodynamic expansion coefficient
σ	Standard deviation of the normal distribution
ρ_a	Density of the adsorbed phase g/cm^3
ρ_b	Density of the gaseous bulk phase, g/cm3
ρ_g	Density of free gas in the bulk phase, g/cm^3
ρ_l	Liquid methane density at boiling point, 422.36 kg/m^3
ρ_c	Liquid methane density at critical point, 162.66 kg/m3
ρ_{vdw}	Methane density calculated by Van der Waals volume, 374.87 kg/m3

Abbreviations

BET	Brunauer–Emmett–Teller
C	Chlorite
EOS	Equation of State
GCMC	Grand Canonical Monte Carlo
GIP	Gas in Place

I	Illite
I/S	Illite-Smectite mixed layer
IEA	International Energy Agency
IUPAC	International Union of Pure and Applied Chemistry
K	Kaolinite
MD	Molecular-Dynamics
PCI	Process Control Interface
S	Smectite
TOC	Total Organic Content
XRD	X-ray Diffraction Analysis

Chapter 1: Introduction

1.1 Overview

1.1.1 Demand for natural gas.

In recent years, natural gas has gained worldwide attention due to the increasing demand of natural gas consumption globally, continuous declining of conventional oil and gas production, widespread availability of unconventional gas reserves, as well as improved technologies to extract it from the ground. In addition, natural gas is also considered as a clean energy option and is favored over other fossil fuels due to its remarkable low environmental impact. As a result of these, there is a fast-growing demand for natural gas all over the world.

As Figure 1-1 shows, the forecasted growth and demand for natural gas in the year 2040 is an enormous amount compared to the demand in the year 2016, especially in the regions of Middle East as well as developing countries, such as China.

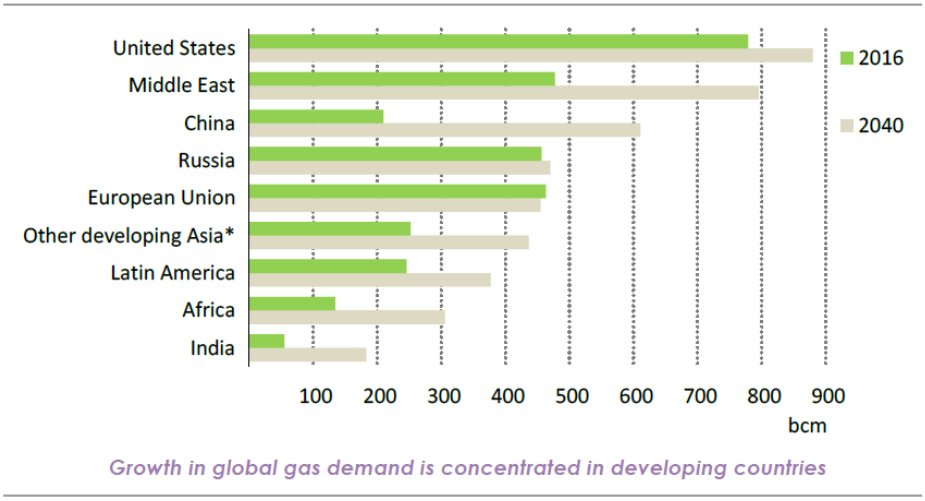

Figure 1-1. Global natural gas demand forecast (Outlook for Natural Gas, 2017)

Despite the vast demand for natural gas energy consumption globally, the production of conventional gas has not been forecasted to increase dramatically in the coming years to meet this demand (Figure 1-2). Nevertheless, the production of unconventional gas is expected to

increase significantly to meet the demand of future natural gas energy consumption. As shown in Figure 1-2, by the year 2040, the expected share of unconventional gas in total natural gas production is estimated at around 33% as compared to only 18% in the year 2013. This increase production of unconventional gas is attributed to many countries in the world. Among them, China, Canada, and the United States of America are expected to increase their unconventional gas production the most. Among these unconventional gas resources, shale gas is considered as one of the primary natural gas sources due to its advantages which will be introduced in the following sub-sections.

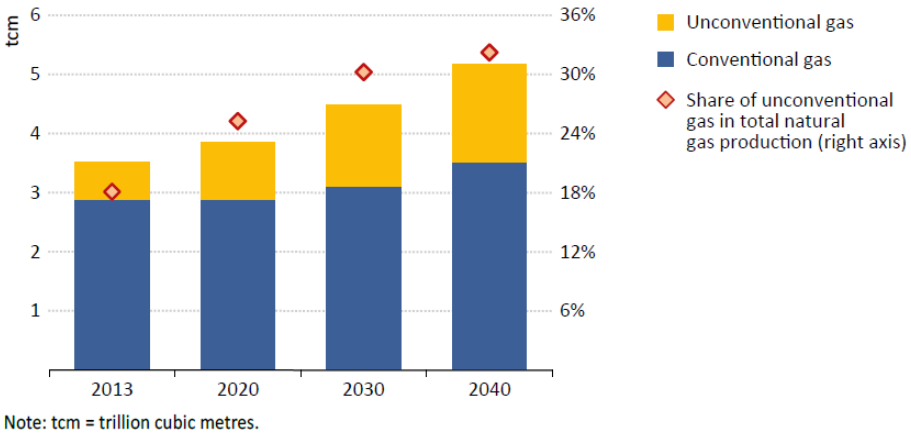

Figure 1-2. Unconventional and conventional gas production forecast (World Energy Outlook, 2015)

1.1.2 Development of shale gas resources.

Shale gas has the most estimated amount available among the unconventional gas resources, which is around 32,600 trillion cubic feet (Aguilera et al., 2014). The vast amount of shale gas scatters around the world in many regions. In the USA, an estimated amount of 862 trillion cubic feet of shale gas is lying underneath the ground (Figure 1-3). Thus, shale gas is considered a valuable energy resource globally due to its enormous amount available (IEA, 2015). Meanwhile, as the horizontal well drilling and hydraulic fracturing technologies have significantly improved in the past decades, the production of shale gas is forecasted to increase

intensely as well. For instance, in the USA, the shale gas production is likely to dominate the total amount of gas produced in the next couple of decades while the other unconventional gas production is decreasing dramatically, as the trends are shown in Figure 1-4.

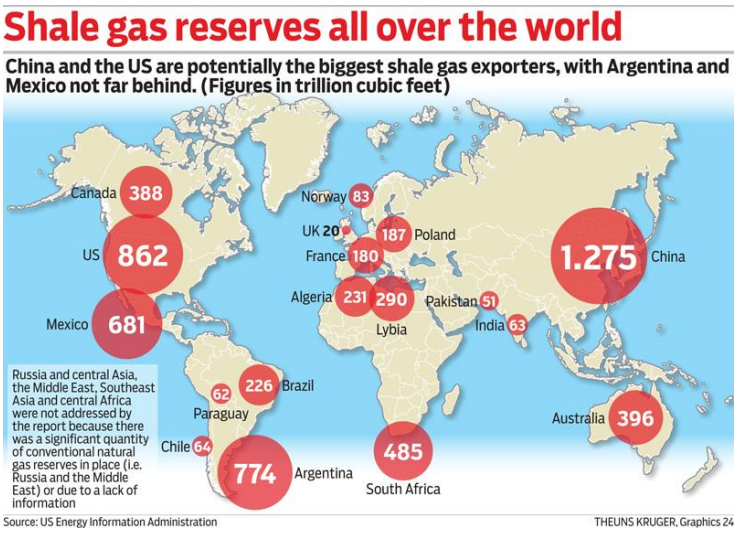

Figure 1-3. Shale gas reserves all over the world (Zhiltsov et al., 2016)

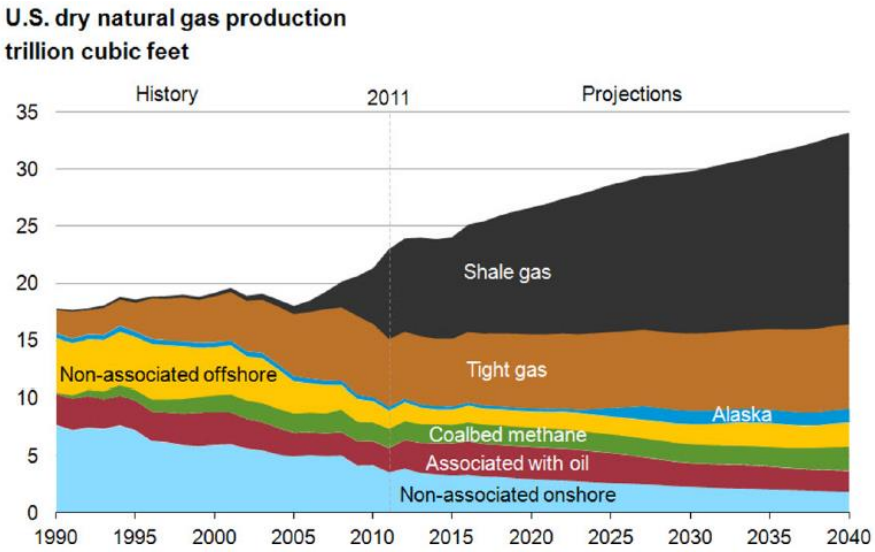

Figure 1-4. U.S dry natural gas production forecast (Saha et al., 2016)

As shale gas is playing an essential role in the future energy supply in the USA as well as globally, it is vital to understand its mineral compositions, pore size distribution, as well as its storage condition to predict a more accurate amount of shale gas reserves available.

1.1.3 Mineral compositions of shale.

The shale rocks are usually made up of a variety of matters, including the organic material, silicate mineral, pyrite mineral, as well as clay, as shown in Figure 1-5.

Different shales are composed of various compositions. As the ternary plot is shown in Figure 1-6-(a), a total of 756 samples of organic-rich shales are analyzed, and most of these shales' compositions include silica mineral as well as clay mineral. Only a minority of these samples is made of carbonate minerals. Figure 1-6-(b), (c), and (d) show the effect of three different deposit environment on shales' composition. As one can see, the marine organic shale contains more carbonate mineral than the marine-continental transitional and Lacustrine ones.

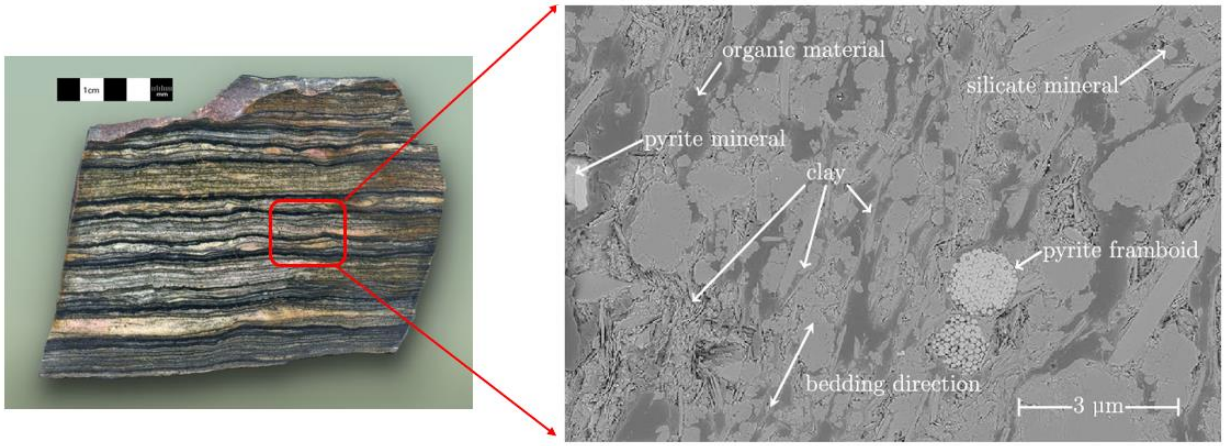

Figure 1-5. Mineral composition of shales (Bennett et al., 2015)

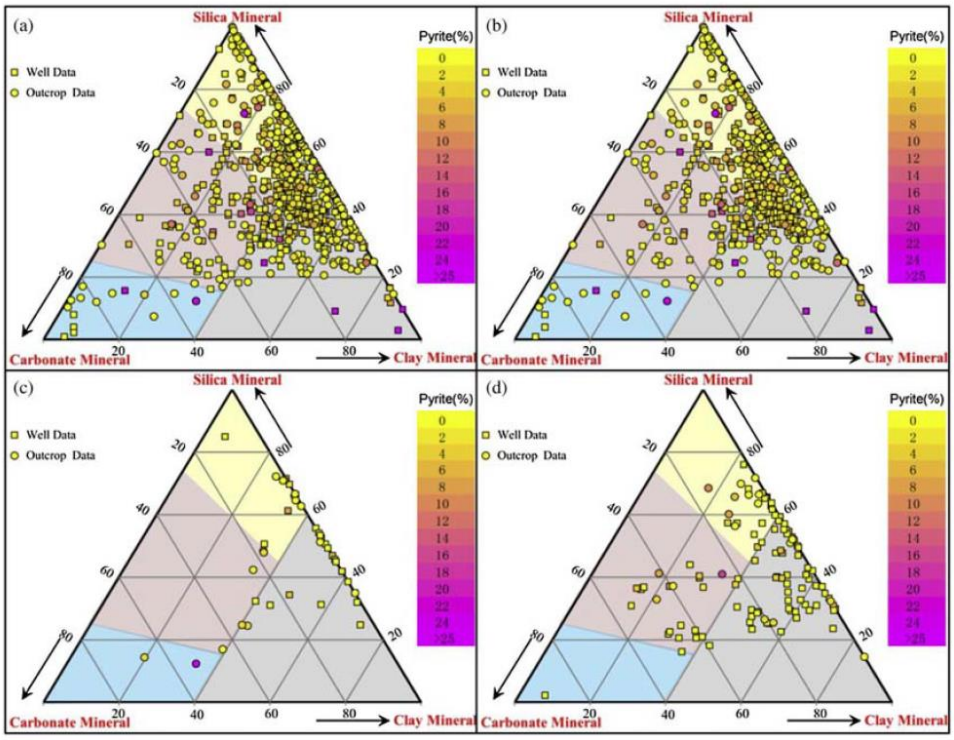

Figure 1-6. Mineral composition of shales comparison (Ju et al., 2014)

Furthermore, the organic matters' adsorption capacity is in a positive correlation with the extent of the organic matter's maturity (Rexer et al. 2014), while each clay material possesses a different adsorption capacity from one another, owing to their various BET (Brunauer-Emmett-Teller) surface areas associated with each clay material (Ji et al. 2012).

1.1.4 Pore size distribution of shale.

The pore size of shale rocks is generally in the range of 0.1 to 0.005 µm, which is considerably smaller than that of a sandstone formation (Figure 1-7). Loucks et al. (2010) presented three main types of pores in shale reservoirs, including pores in organic matter, intraparticle pores in non-organic material, and interparticle pores in non-organic matter (Figure 1-8). The first type, pores in the organic matter, is related to the thermal maturity of the organic matter. Its shape is often irregular. The second type, intraparticle pores in the non-organic material, is associated with both primary grains and particles and secondary dissolution of

calcareous fossils. The third type, interparticle pores in non-organic, is present between the crystals and grains. Different shales possess various pore types. For instance, the Barnett shale samples have about 78% pores in organic matter, while the samples of Pearsall shales only have about 15% intraparticle pores.

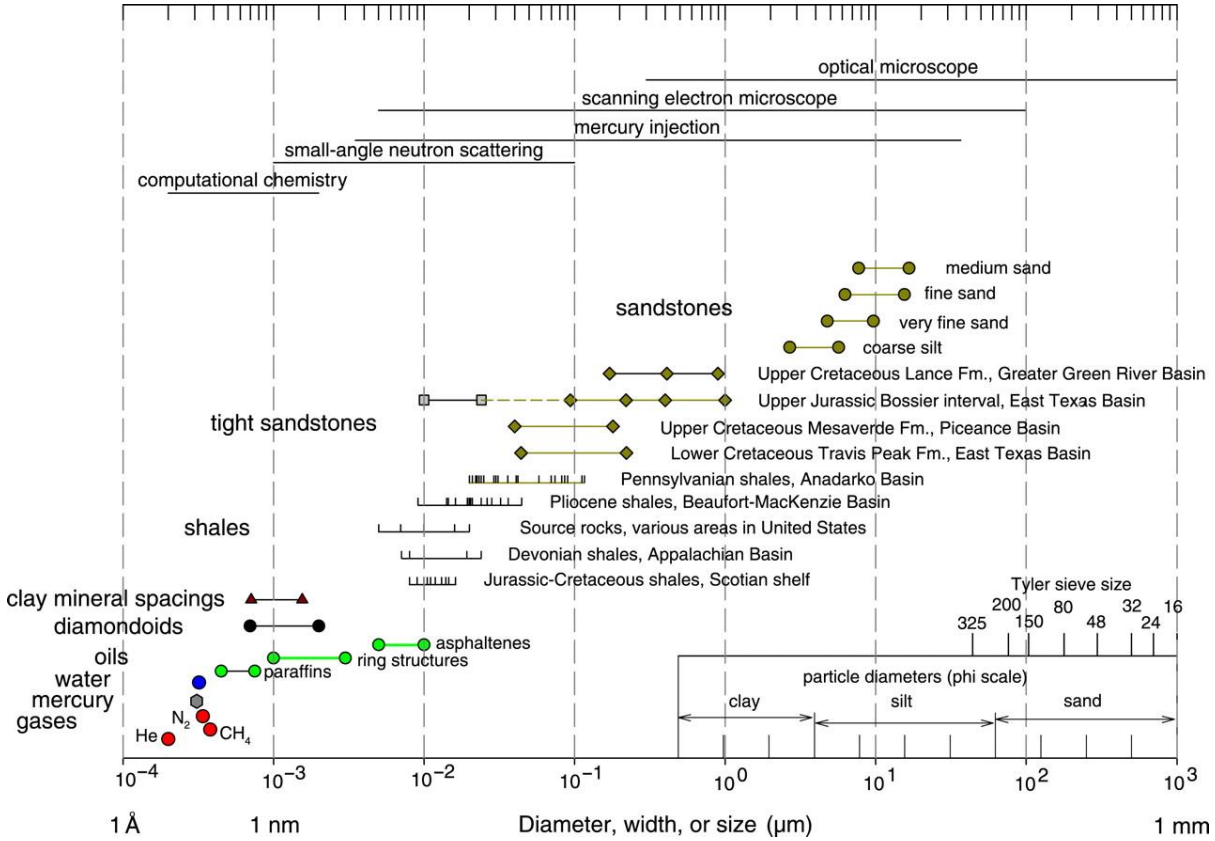

Figure 1-7. Pore sizes comparison chart for various formations (Nelson, 2009)

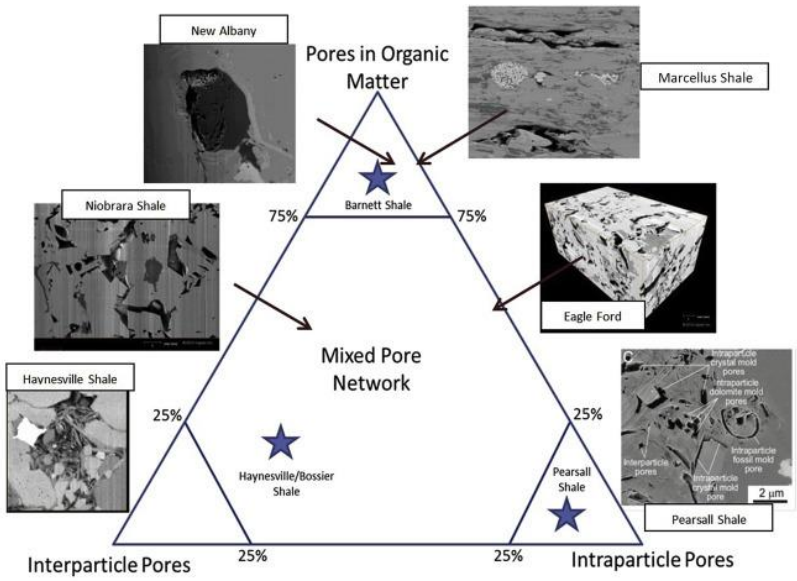

Figure 1-8. The ternary plot for different pore types (Sayed et al., 2017)

1.1.5 Gas storage in shale.

Generally, shale gas mainly exists in a shale reservoir in three forms, free gas in the void space of fractures and matrix, adsorption on the organic matters and clay materials, as well as a dissolved form in bitumen, as illustrated in Figure 1-9. The total gas in place for shales gas reservoir is considered as a sum of free gas and adsorbed gas, because the portion of gas dissolved in the bitumen is often too little to be of any significance. Although the gas molecules could be adsorbed to the surfaces of the fractures, this adsorbed gas amount is negligible compared to the free gas due to the large scale of fractures sizes. Thus, the adsorbed gas within the micro-fractures is always neglected when we consider the storage of natural gas in shales.

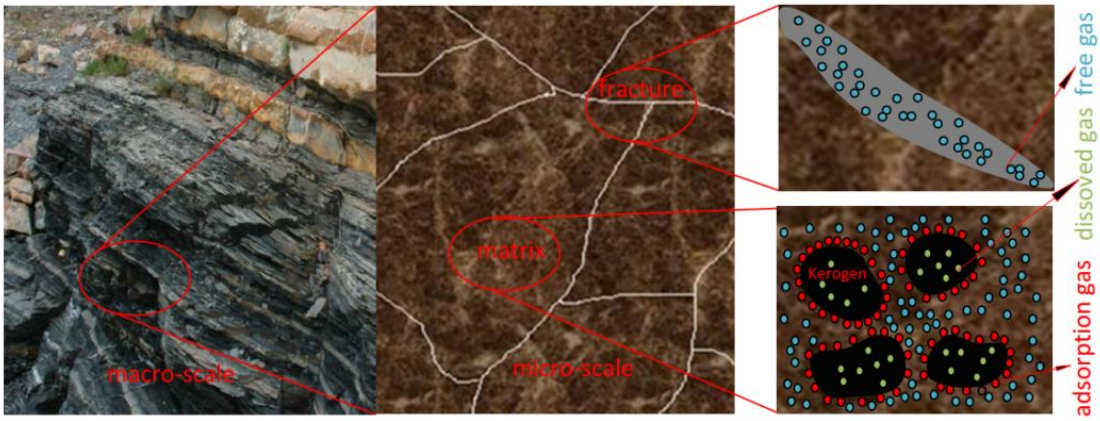

Figure 1-9. Gas distribution in shale reservoirs (Guo et al., 2015)

Among these three forms, the contribution of adsorbed gas to the total gas in place is relatively more significant, as shown in Figure 1-10. As one can see, in this particular case, the portion of the amount of gas in the adsorbed phase is significantly more than that in the free phase. For instance, at 6% TOC, the amount of gas exists in the free gas phase is around 30% of total gas in place comparing to the adsorbed amount of gas which is at around 70%. In fact, some of the shale plays in North America has potentials of 20-85% of total gas in the adsorbed state (Curtis, 2002; Lu et al., 1995). Due to a large amount of gas in the adsorption state, it is critical to understand the nature of adsorption well to have an accurate estimation of the total amount of shale gas in a reservoir (Li et al., 2016).

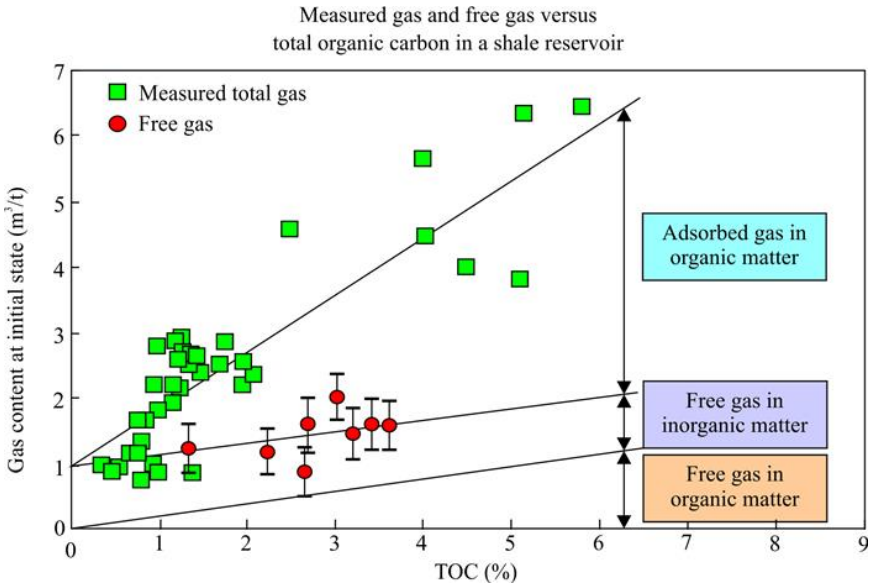

Figure 1-10. Adsorbed gas and free gas in Shale (Wood et al., 2017)

1.1.6 Adsorption model and isotherms.

As discussed above, the composition and pore sizes distribution vary to a great extent for different shales. Yet, the current widely used models for estimating the amount of methane adsorption assume merely homogeneous surface composition, which has a constant value for adsorption heat and standard entropy across a surface. It is hardly the case with the reality as illustrated above. Because of these, a homogenous adsorption model cannot depict the true nature of methane adsorption. Instead, a heterogeneous adsorption model is needed to describe the adsorption behaviors of methane on shales accurately.

Additionally, when it comes to quantifying the amount of adsorbed gas in shale, the current widely used method (Langmuir isotherm) is to consider the absolute adsorption as the actual gas in the adsorbed phase (Zhang et al., 2012; Ji et al., 2012). It is the case when the pressure is low (less than 2 MPa) (Ross and Bustin, 2008). However, as the reservoir pressure goes up, a dramatic difference between the Langmuir isotherm and Gibbs isotherm starts to appear, as shown in Figure 1-11. As a result of that, the application of traditional Langmuir

isotherm under high-pressure conditions would potentially affect the estimation of total gas in place for methane in shales. In order to have an accurate estimation of GIP in shales, a more precise approach should be taken with the notion of Gibbs-excess adsorption (Ambrose et al. 2012).

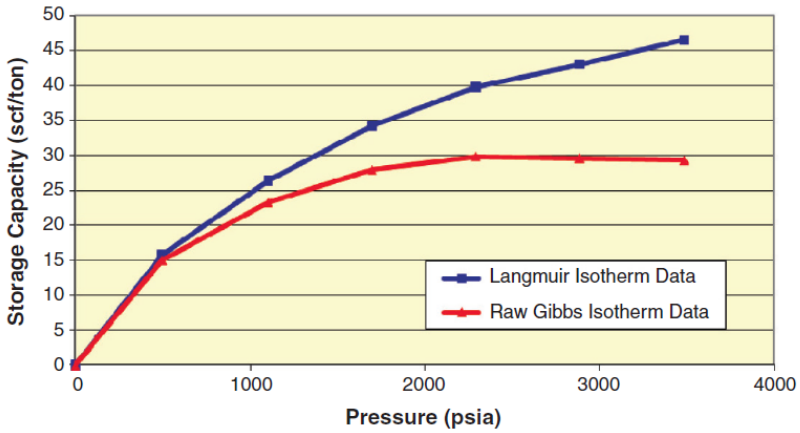

Figure 1-11. Comparison of Langmuir isotherm and raw Gibbs isotherm curves (Ambrose et al., 2012)

1.2 Research Objectives

Methane adsorption on shales is complex in its nature because of these challenges mentioned above. In summary, the following challenges exist in the study of methane adsorption on shales:

- The common misperception exists between the definition of absolute adsorption and excess adsorption;
- The current homogenous adsorption models are unable to characterize the actual methane adsorption process;
- The current method for calculating the total gas in place for shale reservoirs is unable to provide an accurate estimation.

A better understanding of adsorption is needed, and a sophisticated model is required to overcome these challenges to provide an accurate estimation of adsorbed shale gas in place. The primary objectives of this research are as follows:

- To compare and analyze the distinction between absolute adsorption and excess adsorption;
- To propose a multi-site adsorption model to address the heterogeneity of shales;
- To find an accurate method for calculating the total gas in place for shale reservoirs with the derived multi-site adsorption model and analyze the parameters that affect the GIP.

1.3 Thesis Organization

This thesis consists of six chapters in total. The organization of this thesis and description for each chapter is provided as follows:

In Chapter 1, we provide an overview and introduction of the thesis's topic.

In Chapter 2, we review the current literature available related to the topic. In this chapter, the definition of adsorption, both the absolute adsorption and excess adsorption are introduced and compared. Four methods of calculating the adsorbed phase density are introduced as well. Two experimental methods for measuring the adsorption isotherms are discussed. A comparison of absolute and excess adsorption isotherms is made, and their differences are compared and analyzed.

In Chapter 3, we review the current traditional adsorption models and discuss their shortcomings unable to address the heterogeneity of shales. A step by step approach of deriving a multi-site model for both absolute and excess adsorption is carried out in this chapter to depict

the heterogeneous energetic nature of shales. Relevant assumptions in the derivation of equations are made and discussed as well.

In Chapter 4, we introduce the procedures for conducting adsorption experiments and demonstrate the fitting results with the traditional single-site adsorption model and multi-site adsorption model. A comparison of the results is made in terms of accuracy with the experimental data. Furthermore, the absolute adsorption and excess adsorption isotherms are also compared and analyzed.

In Chapter 5, we discuss the application of the derived adsorption models in calculating the total gas in place for shale reservoirs. Both the absolute adsorption method and the excess adsorption method are utilized and compared. An accurate method for GIP calculations is chosen, and a sensitivity analysis is carried out to investigate the effect of several parameters of reservoir properties on GIP.

In Chapter 6, we provide major conclusions of this thesis and future recommendations.

Chapter 2: Absolute Adsorption and Excess Adsorption

2.1 Definition of Adsorption

The term adsorption is first brought up by Kayser in 1881 to address the phenomenon that has been recognized by Fontana and Scheele in 1777 and described as the process of increasing concentration of gas molecules towards the adjacent solid surfaces (Roque-Malherbe, 2007). The adsorption process is mainly caused by a weak Van der Waals force between gas molecules and a solid surface, which is classified as physisorption (Ji et al., 2012; Yang et al., 2015).

There are generally two terms used for describing the adsorbed phase in porous media. One is called absolute adsorption, which is defined as the total amount of gas in the adsorbed state in porous media (Do et al., 2010). The concept of absolute adsorption takes an adsorbed layer into account, as shown in Figure 2-1-a. The other term used to describe the adsorption is called excess adsorption, which is introduced by Gibbs (1931). On the contrary to the absolute adsorption, the definition of excess adsorption does not take an actual adsorbed layer volume into account, as shown in Figure 2-1-b. In the Gibbs model of adsorption, a dividing surface is replacing the actual interface between the bulk gas phase and the solid instead (Myers, 2012).

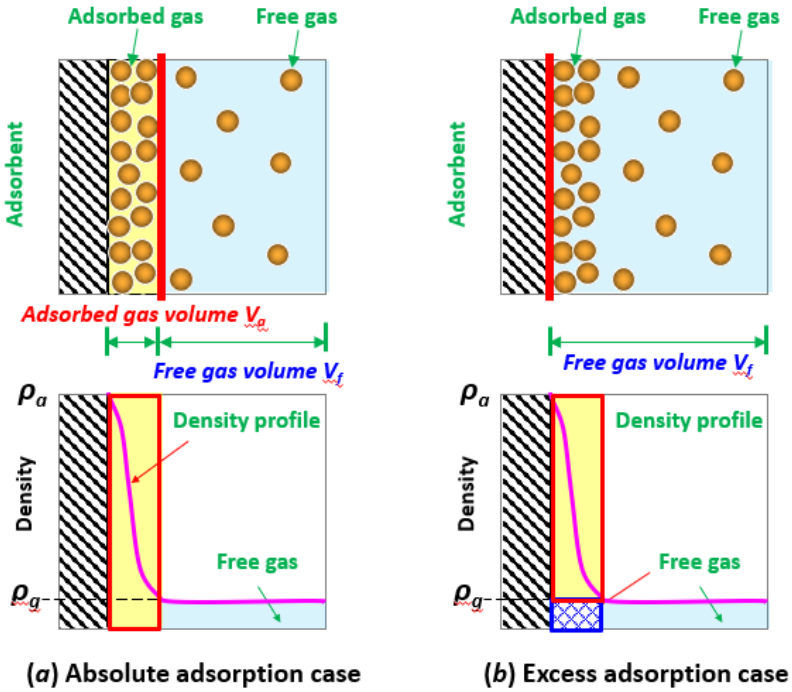

Figure 2-1. Illustration of (a) absolute adsorption case and (b) excess adsorption case

Furthermore, the equation of absolute adsorption is a function of the adsorbed phase volume and the adsorbed phase density, as Figure 2-2 demonstrates, shown as follows:

$$n_{ab} = \frac{V_a * \rho_a}{M} \tag{2.1}$$

where n_{ab} is the absolute adsorption amount, g/cm^3; V_a is the volume of the adsorbed phase, cm^3/g; ρ_a is the density of the adsorbed phase g/cm^3.

The relationship between the absolute adsorption and excess adsorption can be clearly illustrated by Figure 2-2 as well; as one can see in this figure, the excess adsorption amount is included in the absolute adsorption amount. Therefore, the equation for excess adsorption is subtracted from the absolute adsorption equation, shown as follows:

$$n_{ex} = \frac{V_a * \rho_a}{M} - \frac{V_a * \rho_g}{M} \tag{2.2}$$

where ρ_g is the density of free gas in the bulk phase, g/cm^3.

By substituting equation (2.1) into equation (2.2), another expression of excess adsorption can be obtained as follows:

$$n_{ex} = n_{ab} * (1 - \frac{\rho_g}{\rho_a}) \tag{2.3}$$

where ρ_a is the constant value that represents the adsorbed phase density.

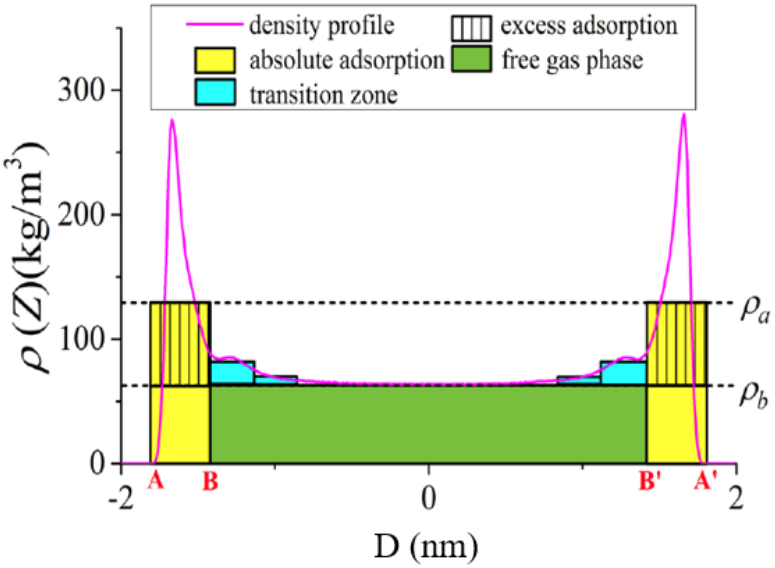

Figure 2-2. Comparison of density profile of absolute adsorption and excess adsorption (Tian et al., 2017)

2.2 Bulk Phase Density

As it is shown in equation (2.3), the value of the bulk phase density is essential in determining the excess adsorption value. The bulk phase density denoted as ρ_g is often calculated using the method named an equation of state (EOS). The EOS method is used to calculate the bulk phase density of the gas at specific pressure and temperature. There are, in fact, several various EOS methods available for that purpose. Among them, the most commonly applied ones are the cubic equations of Peng-Robinson (PR), the multiparameter Setzmann and Wagner (Se-W), as well as the Redlich-Kwong (RK). In this thesis, the RK EOS method (Redlich and Kwong, 1949) is chosen for the calculation of ρ_g due to its accuracy of prediction

under high temperature and high pressure conditions (Wu et al., 2016), which is also the case in most shale reservoir conditions. The RK EOS equations are shown as follows:

$$\rho_g = \frac{MP}{ZRT} \tag{2.4 a}$$

$$P = \frac{RT}{V-b} - \frac{a}{V(V+b)} \tag{2.4 b}$$

$$V = \frac{ZRT}{P}; a = \frac{0.42748*R^2T_c^{2.5}}{T^{0.5}P_c}; b = \frac{0.08664*RT_c}{P_c} \tag{2.4 c}$$

where M is the molar mass of methane, g/mol; Z is the compressibility factor of methane in the gas phase; V is the molar volume of methane, cm^3/mol; T_c is the critical temperature of methane, K; P_c is the critical pressure of methane, MPa; a and b are the parameters in the RK-EOS method.

From Figure 2-3, it can be seen that the results calculated by the RK-EOS method are matching reasonably well with the data from other published works (Zhu and Zhao, 2014; Zhang et al., 2016). Therefore, this EOS method is considered applicable for the calculation of ρ_g in this work.

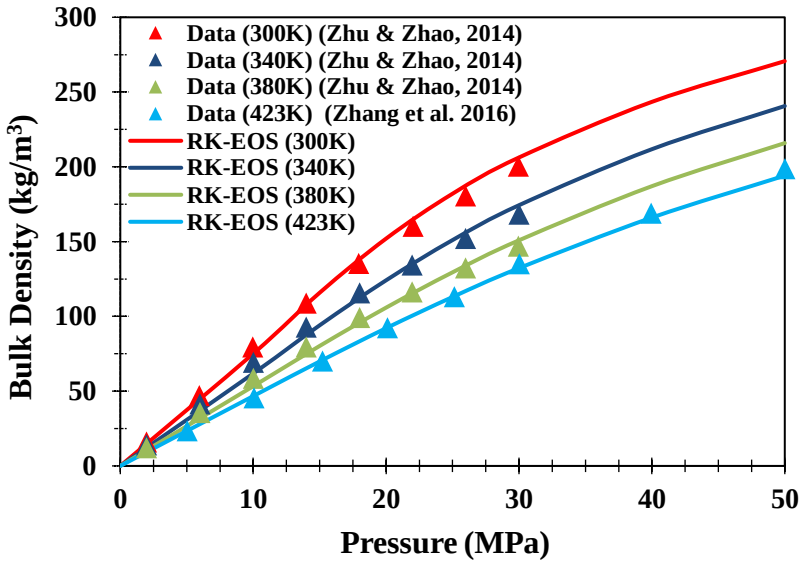

Figure 2-3. The comparison of the gaseous methane density between the results of RK-EOS and molecular simulation data from other published works (Li et al., 2018)

2.3 Adsorbed Phase Density

As one can see from the equation introduced in Section 2.1, the adsorbed phase density is critical regarding evaluating the excess adsorption. The adsorbed phase density of excess adsorption is quite distinct with the one of absolute adsorption. As illustrated in Figure 2-1-a, under the absolute adsorption situation, the adsorbed phase density profile varies across the interface. However, in the excess adsorption case shown in 2-1-b, the adsorbed phase density profile is taken place by the Gibbs dividing surface, and the adsorbed phase density is instead a set value than a variable in this case. Nevertheless, it is difficult to measure the value of the adsorbed phase density directly. Generally, there are four methods that are commonly applied to solve this problem.

2.3.1 Direct fitting method.

One of the conventional methods is to obtain the adsorbed phase density through direct fitting with experimentally measured adsorption isotherms (Rexer, et al., 2014; Gasparik et al., 2014). Despite the prevalent use of this method, it does have one shortcoming, which is that the results generated by this curve fitting method are too broad to be applicable for any real purposes. In some cases, the estimated value of the methane adsorbed phase density can reach up to 800 g/cm^3 (Shabani et al., 2018), as shown in table 2-1. This value is larger than the solid methane density. Therefore, it has no physical meaning associated with it anymore.

Table 2-1. Results of methane density at various temperatures calculated by the direct fitting method (Shabani et al., 2018)

Type	Temperature (^{0} C)	n_{ex}^{10MPa}	n_∞ (mmol/g)	P_L (MPa)	ρ_a (kg/m^3)
G1	45	0.022	0.04	5.1	399.1
	70	0.019	0.04	8.23	399.1
	100	0.015	0.04	12.62	399.1
	130	0.015	0.04	13.43	399.1
G7	45	0.045	0.058	1.9	777.3
	70	0.042	0.058	2.89	777.3
	100	0.032	0.058	7.09	777.3
	130	0.027	0.058	10.14	777.3

G10	45	0.075	0.109	2.55	523.4
	70	0.063	0.109	5.19	523.4
	100	0.057	0.109	7.12	523.4
	130	0.044	0.109	12.25	523.4
G11	45	0.051	0.079	3.28	498.4
	70	0.048	0.079	4.47	498.4
	100	0.041	0.079	7.04	498.4
	130	0.031	0.079	12.77	498.4
S3	45	0.107	0.13	3.18	769.8
	70	0.091	0.13	3.18	769.8
	100	0.087	0.13	3.97	769.8
	130	0.07	0.13	7.35	769.8
S4	45	0.2	0.29	2.46	491.8
	70	0.173	0.29	4.74	491.8
	100	0.127	0.29	10.29	491.8
	130	0.115	0.29	12.78	491.8
S6	45	0.089	0.124	2.4	618
	70	0.077	0.124	4.51	618
	100	0.069	0.124	6.51	618
	130	0.06	0.124	8.93	618
S8	45	0.213	0.257	1.04	823.4
	70	0.194	0.257	2.26	823.4
	100	0.163	0.257	4.67	823.4
	130	0.139	0.257	7.34	823.4

2.3.2 Constant value approach.

Another prevalent method is to treat the value of adsorbed phase density as a constant. Usually, the liquid methane density is used for this value (Yang et al., 2015). This method, however, cannot be applicable in all cases. As shown in Figure 2-4, 6 cases of measured excess adsorption data are used for fitting with a three-parameter Langmuir-based excess sorption function as well as a fixed value of liquid methane density for comparison. As the results show above, out of the 6 cases, 5 of them generate acceptable fitting results with the 2 values of adsorbed phase densities (1 calculated value and 1 constant value of the liquid methane density) except the last case (Gasparik et al., 2012). This result shows that merely assuming a liquid methane density as the adsorbed phase density does not work in all cases.

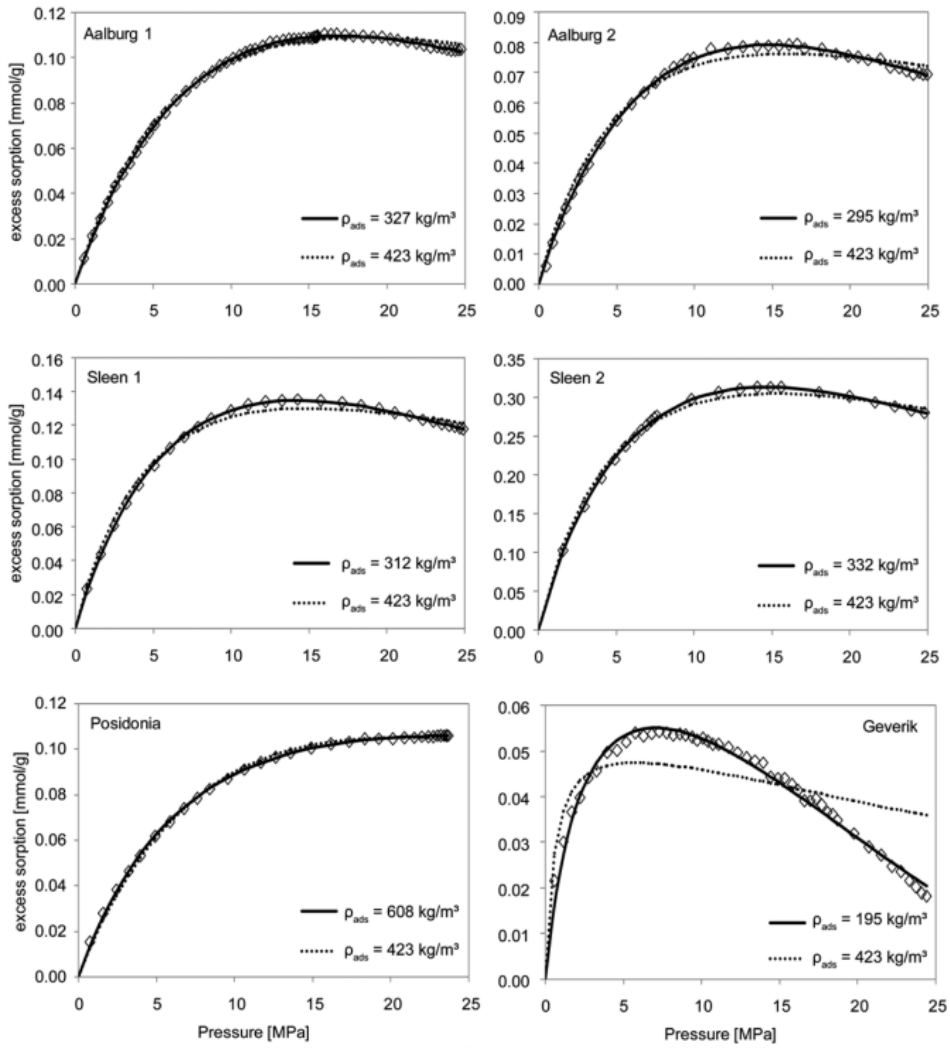

Figure 2-4. Excess sorption isotherms with fitted three-parameter sorption function and constant methane density (Gasparik et al., 2012)

The reason behind the fact that assuming one fixed value of an adsorbed phase density, such as the liquid methane density, is not applicable in all cases is that, under different temperatures, the adsorbed phase densities are different (Charoensuppanimit et al., 2015). When the temperature increases, the adsorbed phase expands, and the methane molecules packing becomes less dense than that of the ones at lower temperatures (Do, 1998). The phenomenon is referred to as the thermal expansion effect (Yang et al., 2017). Hence, the value of an adsorbed phase density is a temperature-dependent value. Therefore, it is inappropriate to treat the

adsorbed phase density as a constant, especially in high-temperature conditions, which is the case with most shale reservoirs.

2.3.3 Simulation method.

Other than the two methods listed above for obtaining the adsorbed phase density, in recent years, many researchers have applied methods of molecular-dynamics (MD) simulations as well as grand canonical Monte Carlo (GCMC) simulations to find the value of the adsorbed phase density (Ambrose et al., 2012; Tian et al., 2017). The simulation results from the MD simulations are in the range of 259 g/cm^3 to 307 g/cm^3, while the GCMC simulations yield results in the range of 209 g/cm^3 to 265 g/cm^3. As one can see from Figure 2-5, three various cases of pore width are simulated with the MD simulation method; this graph shows the simulated results of adsorbed phase densities are within the ranges mentioned earlier. The range and values of those results are smaller than those generated by a curve fitting method. Therefore, the results generated by the simulation method possess physical meaning. However, due to the fact that simulation work is complicated and takes an enormous amount of time, simplified approximation methods are sometimes preferred to calculations of the adsorbed phase densities.

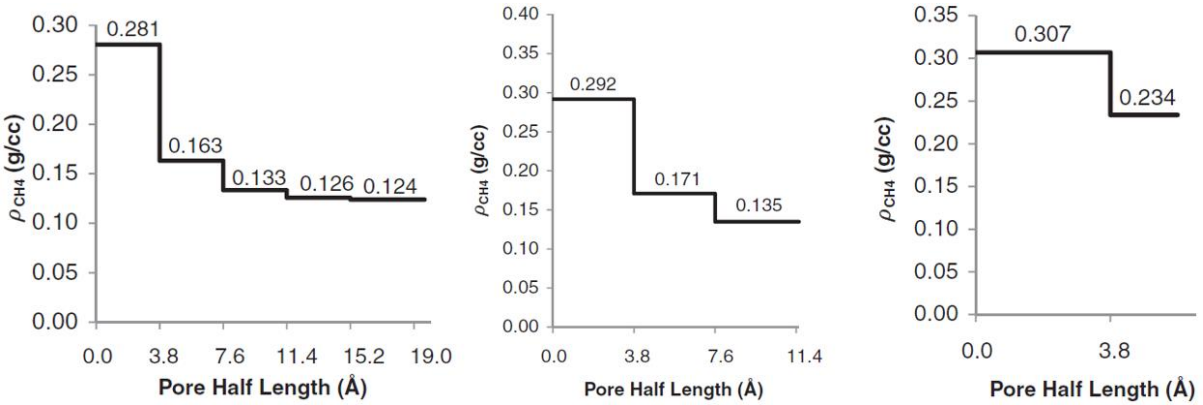

Figure 2-5. Methane density simulation results for three cases (Ambrose et al., 2012)

2.3.4 Theoretical calculation method.

Table 2 shows a list of the methods that have been used to approximate the values of the adsorbed phase density. However, some of these methods do not consider the effect of temperature, as one can see in Table 2. For instance, Nikolaev and Dubinin (1958) regarded the adsorbed phase density as a constant and it is the inverse of the Van der Waals volume. Reich et al. (1980) regarded the adsorbed phase density as the liquid density at the boiling point, and Mehta and Danner (1985) regarded the adsorbed phase density as the liquid density at the critical point. Meanwhile, some other methods take account of the effect of temperature when it comes to approximate the adsorbed phase density. For instance, in the equation proposed by Ozawa et al. (1976), it is noted that the adsorbed phase density decreases as temperature increases. This is caused by the thermal expansion effect mentioned above. As discussed earlier, taking account of the thermal expansion effect in an adsorbed phase density provides the benefit of bringing more physical meaning to the adsorption phenomenon than treating the adsorbed phase density as a constant. Besides, another benefit of considering the thermal expansion effect with an adsorbed phase density is such that better results of adsorption isotherms curves will be generated than that of the ones with a constant adsorbed phase density (Yang et al., 2017). Because of these benefits, the equation proposed by Ozawa et al., shown in the following, will be used in the next section to calculate the adsorbed phase density:

$$\rho_a = \rho_l * e^{-\lambda(T-T_b)} \tag{2.5}$$

where, ρ_l is the liquid methane density at boiling point, 422.36 kg/m^3; λ is the thermodynamic expansion coefficient, and, in this thesis, the value of 2.5x10^{-3} is applied, unit of K^{-1}. A detailed

explanation of this coefficient and its application will be discussed in the following chapters; T_b is the boiling temperature of methane, 111.66 K (Setzmann and Wagner, 1991).

Table 2-2. Summary of several simplified calculation methods for adsorbed phase density (Li et al., 2018)

Temperature	Approximation	Relationship	References
$T<T_c$	Density of Saturated liquid	Eq.(3.4) in Setzmann & Wagner's work	Setzmann & Wagner, 1991
	Liquid density at boiling point	$\rho_a^* = \rho_l$	Relch et al., 1980
	Linear approximation	$\rho_a^* = \rho_l - (\rho_l - \rho_{vdw})(\frac{T-T_b}{T_c-T_b})$	Dubinin, 1960
	Superheated liquid	$\rho_a^* = \rho_l \cdot e^{-\lambda(T-T_b)}$	Ozawa et al., 1976
$T>T_c$	Liquid density at boiling point	$\rho_a^* = \rho_l$	Relch et al., 1980
	Liquid density at critical point	$\rho_a^* = \rho_c$	Mehta & Danner, 1985
	Inverse of Van der Waals volume	$\rho_a^* = \rho_{vdw} = \frac{8MP_c}{RT_c}$	Nikolaev & Dubinin, 1958
	Superheated liquid	$\rho_a^* = \rho_l \cdot e^{-\alpha(T-T_b)}$	Ozawa et al., 1976

2.4 Adsorption Isotherms

2.4.1 Adsorption isotherms measured in experiments.

In general, there are two experimental methods to measure the adsorption isotherms of methane on shale rocks; one is gravimetric, and the other is called the volumetric method (Murata et al., 2001). The gravimetric method measures the excess adsorption capacity based on the differences between gravity and buoyancy. However, due to the difficulty of assessing the buoyancy accurately, this method may be unsuitable for measuring the total adsorption amount on a surface (Tian et al., 2017). The volumetric method is commonly used when it comes to studying the isotherms of methane adsorption (Tian et al., 2017; Liu et al., 2018). The adsorbed phase volume cannot be measured. Instead, the volumetric method measures the excess uptake amount of methane adsorption. The adsorbed phase amount is measured as the difference between the total gas amount and the bulk gas phase amount. The equation to illustrate the relationship of the volumetric method measurements results is as follows:

$$n_a = n_T - n_b \tag{2.6}$$

where n_a is the adsorbed gas amount, mol/g; n_T is the total gas amount, mol/g; n_b is the bulk gas amount, mol/g. The equation for n_b is as follows:

$$n_b = \frac{V_T * \rho_b}{M} \tag{2.7}$$

where V_T is the total volume of the measurement system, cm3/g; ρ_b is the density of the gaseous bulk phase, g/cm3; M is the molar mass of the adsorbent, g/mol.

Figure 2-6 demonstrates the graphic relationship of these terms used in the above equations. The total volume of regions of A, B, and C represents the value of total gas amount, n_T. The sum volume of regions B and C represents the value of bulk gas amount, n_b. Consequently, the volume of region A equals the adsorbed gas amount, n_a, which is also the Gibbs excess adsorption uptake.

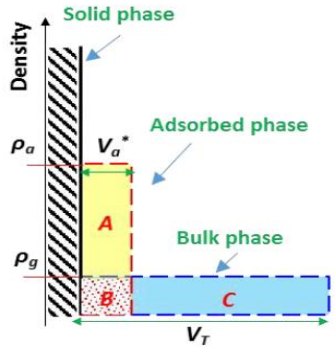

Figure 2-6. Schematic of adsorbed phase and bulk phase (Li et al., 2018)

2.4.2 Comparison of absolute and excess adsorption isotherms.

As it is shown in Figure 2-7, in a 1 nm pore at 298 K, up to 1.5 MPa, the absolute adsorption and excess adsorption are almost identical; however, once it passes 1.5 MPa, as the pressure continues to increase, the difference between the absolute adsorption and excess adsorption starts to become progressively clear and significant.

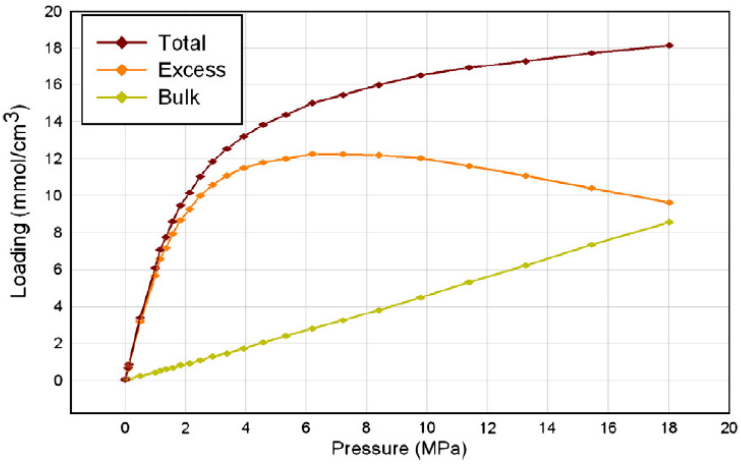

Figure 2-7. Comparison of Langmuir isotherm with excess adsorption isotherm (Mosher et al., 2013)

As one can see in this figure, the absolute isotherm curve continues to increase as pressure goes up. This type of curve is referred to as Langmuir curve. The Langmuir curve is associated with the classical Langmuir model, which assumes monolayer adsorption on shale rock surfaces (Zhang et al., 2012; Ji et al., 2012). The reason that a Langmuir curve is believed to be representing the phenomenon of adsorption by early researchers is that most of those early adsorption experiments were carried out under relatively low-pressure conditions (less than 10 MPa), and, consequently, the results obtained from those experiments matched well with the type of curve of the classical Langmuir model (Lu et al., 1995, Ji et al., 2012).

However, under the shale reservoirs conditions, a high-pressure scenario almost always exists, and, in fact, some of them can reach about 35 MPa (Dong et al., 2013). Therefore, it is critical to understand the adsorption phenomenon under such high-pressure conditions to comprehend a full picture of adsorption behaviors in reality. To achieve this goal, subsequent researchers have conducted simulations work as well as experimental research to find out the adsorption behaviors under high-pressure scenarios (larger than 20 MPa). Unlike the shape of the absolute adsorption isotherm curve, what they have found out is that the excess adsorption

uptake of methane reaches a maximum peak value and then drops down afterward as the pressure continues to increase, just like the parabola curve of excess adsorption shown in Figure 2-7 (Mosher et al., 2013; Tang et al., 2016). Therefore, it is clear that a direct application of the classical Langmuir model to describe the adsorption phenomenon ends up overestimating the uptake of methane adsorption (Ambrose et al., 2012).

2.4.3 Confusion between absolute and excess adsorption.

The reason for identical isotherm curves of absolute and excess adsorption under low-pressure conditions can be explained by the excess adsorption equation. As shown in the equation (2.3), n_{ex} is a function of n_{ab} and $(1 - \frac{\rho_g}{\rho_a})$. Therefore, the magnitude of $\frac{\rho_g}{\rho_a}$ is essential in determining whether the value of n_{ex} is close to that of n_{ab}. The two factors that affect the magnitude of $\frac{\rho_g}{\rho_a}$ are pressure and temperature. To understand better how pressure and temperature affect the magnitude value of $\frac{\rho_g}{\rho_a}$, the relationship between the value of $\frac{\rho_g}{\rho_a}$ and the pressure is generated with the help of the equation proposed by Ozawa et al. for the adsorbed phase density, as shown in Figure 2-8.

Firstly, the value of the bulk phase density is calculated using equation (2.4 a, b, c) at various pressure and temperature conditions; then equation (2.5) is applied to calculate the adsorbed phase densities at those temperature conditions. Finally, we plot the value of $\frac{\rho_g}{\rho_a}$ versus pressure under various temperature conditions, as shown in Figure 2-8-a. Similarly, we repeat the above procedures for another set of pressure and temperature conditions, and generate the plot of the value of $\frac{\rho_g}{\rho_a}$ versus temperature under various pressure conditions, as shown in Figure 2-8-b.

In low-pressure conditions, the value of ρ_g, the bulk phase density, is relatively insignificant compared to the value of the adsorbed phase density ρ_a. Therefore, the value of $\frac{\rho_g}{\rho_a}$ is negligible in the equation, which brings the value of $(1 - \frac{\rho_g}{\rho_a})$ almost equal to 1, which can be seen from Figure 2-8-a. As a result, the absolute adsorption value is nearly the same as the excess adsorption. However, as the pressures increases, as one can see from Figure 2-8-a, the value of $\frac{\rho_g}{\rho_a}$ is no longer a non-negligible and starts to increase dramatically. Other than pressure, temperature also plays its role of affecting the value of $\frac{\rho_g}{\rho_a}$. As it shows in Figure 2-8-b, under 6 various pressure conditions, as the temperature increases from 250 K to 400 K, the value of $\frac{\rho_g}{\rho_a}$ starts to drop except the 2 cases with low pressure circumstances (P=0.1 MPa and P=1 MPa). As the dash line indicated in Figure 2-8-b, the value of $\frac{\rho_g}{\rho_a}$ starts to become significant and cannot be ignored any more $(\frac{\rho_g}{\rho_a} = 0.01)$ once the pressure passes 1 MPa. That is when the absolute adsorption isotherms and excess adsorption isotherms start to look progressively different in shapes.

Another thing to note in this figure is that the effect of increasing temperature is relatively less significant compared with the effect of pressure on the value of $\frac{\rho_g}{\rho_a}$. The reason for the little effect of temperature can be explained by Figure 2-9 shown below. As one can see in this figure, the adsorbed phase density decreases as the temperature increases. Similarly, the bulk phase densities at various pressure conditions also decrease as the temperature continues to increase. Since both values are in the trend of decreasing as the temperature increases, the value of their ratio stays relatively unaffected by the changes of the temperature.

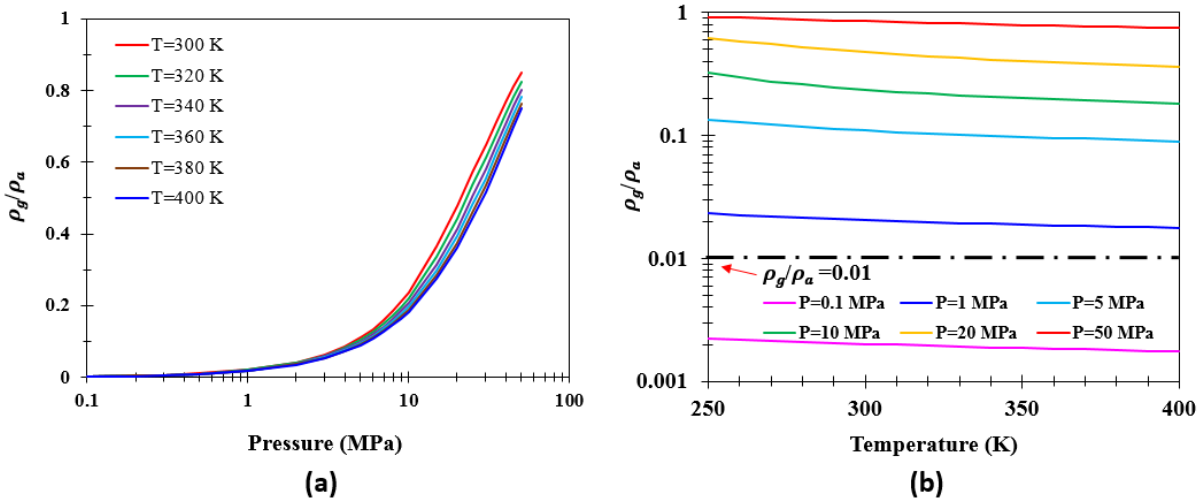

Figure 2-8. (a) The effect of pressure on the magnitude of $\frac{\rho_g}{\rho_a}$ (b) the effect of temperature on the magnitude of $\frac{\rho_g}{\rho_a}$

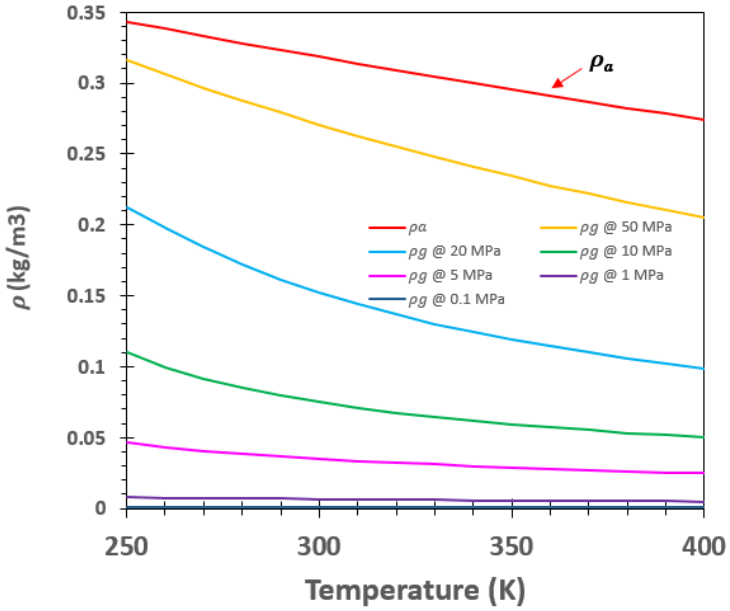

Figure 2-9. The effect of temperature on adsorbed phase density and bulk phase density

2.5 Summary

In this chapter, we discuss the fundamental concepts of absolute adsorption and excess adsorption. Their differences are compared and analyzed in terms of derivation of their formulas as well as their isotherm figures. The following conclusions can be drawn:

- The fundamental difference between absolute adsorption and excess adsorption is whether the adsorbed layer volume is considered in their definition; the excess adsorption assumes a Gibbs dividing surface that takes no volume instead of the actual adsorbed layer in the absolute adsorption case. Thus, the absolute adsorption is always more substantial than the excess adsorption, and their difference can be characterized by the bulk gas phase amount that takes up the adsorbed phase volume.
- There are a few methods available for calculating the adsorbed phase density, including the direct fitting and constant value approaches, simulation methods, and theoretical calculation methods. Among them, the theoretical calculation method approach is considered to be the most appropriate one to use in this work. It possesses the advantages of considering the thermal expansion effect, accuracy of the calculation results, as well as efficiency comparing with the other methods.
- The absolute adsorption isotherm increases progressively as the pressure goes up, while the excess adsorption isotherm behaves like a parabolic curve, continuing to increase to a maximum and then drops as the pressure continues going up. The reason behind this phenomenon can be explained by the relative value of $\frac{\rho_g}{\rho_a}$ under various pressures. Only in low pressure conditions (e.g., less than 1 MPa), $\frac{\rho_g}{\rho_a}$ is negligible (e.g., less than 0.02), and these two adsorption isotherm curves looks almost identical.

Chapter 3: Single-site and Multi-site Adsorption Model

3.1 Absolute Adsorption Models

As discussed in Chapter 2, adsorption isotherms illustrate the relationship between the amounts of adsorbate adsorbed onto an adsorbent with a pressure change as temperature stays the same. For absolute adsorption, due to the various characteristics of adsorbate and adsorbent (e.g., the strength of an adsorbate-adsorbent interaction), generally, there are six types of adsorption models available according to the IUPAC classification to depict its adsorption behaviors (Donohue and Aranovich, 1998). These six types of adsorption models are demonstrated in Figure 3-1 below.

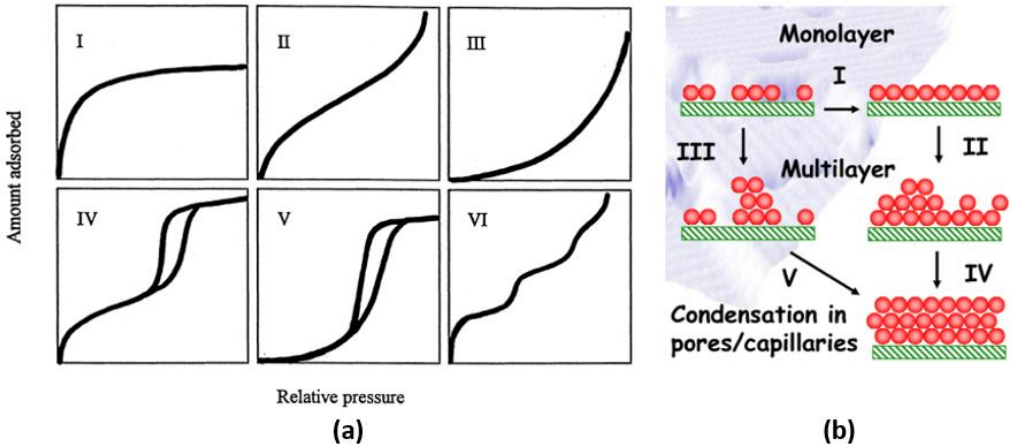

Figure 3-1. (a) Six types of adsorption models (b) adsorbate and adsorbent interactions of various types of adsorption isotherms (Donohue and Aranovich, 1998)

Each of these six isotherm curves represents a variety of scenarios for absolute adsorption phenomenon. Type I is the most common type, as shown in the above Figure a-I, this type has been introduced in Chapter 2, and it is also referred to as the Langmuir curve. It is a monotonic growing line as the pressure increases until it reaches a specific limiting value. This type of isotherm curve is usually applied to illustrate the adsorption process that involves a monolayer of adsorption, as shown in Figure 3-1-b. In the case of a multi-layer of adsorption, type II and type

III are used to describe these adsorption processes. The differences in the curve shapes of type II and type III shown in Figure 3-1-b can be explained by the differences in the magnitude of the interactions between the adsorbate and the adsorbent of type II and type III isotherms. In this case, type II isotherm has a relatively strong interaction of adsorbate and adsorbent and thus the way the adsorbate adsorbing onto the adsorbent follows the sequence of binding the first layer first, then moving onto the second one, binding the second layer, then moving onto the third one, and continuing like this. Unlike the type II isotherm, type III isotherm has a relatively strong interaction among adsorbates themselves, and thus the adsorbates tend to bind onto each other first and then adsorb onto the adsorbent surface. As a result, before the formation of the second adsorption layer, this type of isotherm (type III) has had adsorbates bound with each other rather than filling up the full layer on the adsorbent first, as the scenario is shown in Figure 3-1-b for type III. As the packing of the adsorbate becomes dense and as the condensation in pores and capillaries happens, type IV is used to replace type II while type V is replacing type III to demonstrate the adsorption behaviors. Type VI is also known as the step-wise isotherm and shows the multiple steps for the adsorption to take place in some adsorbent and adsorbate cases.

Other than the isotherm curves to represent the absolute adsorption process, there are also mathematical equations available to describe the absolute adsorption behaviors. Table 3-1 below summarizes a list of some common equations that are used for this purpose.

Table 3-1. List of equations commonly used for describing absolute adsorption isotherms

Name	Isotherm Equation	Symbols	Application
Henry	$n_{ab} = kP$	n_{ab} is the adsorption amount, mol/g; k is Henry's constant, MPa^{-1}; P is equilibrium pressure for adsorption, MPa.	This linear equation between the adsorption amount and equilibrium pressure is applicable only under low-pressure conditions.
Langmuir	$n_{ab} = n_{max}\frac{P}{P_L + P}$	n_{max} is the maximum adsorption capacity, mol/g; P_L is the Langmuir pressure, MPa.	The Langmuir equation is commonly used to describe the type I isotherm curves.

BET	$\frac{P/P_0}{V(1-\frac{P}{P_0})} = \frac{1}{cV_m} + \frac{c-1}{cV_m}(\frac{P}{P_0})$	P_0 is the saturation pressure of adsorbates at the temperature of adsorption, MPa; V is the volume of the adsorption amount; V_m is the volume of the monolayer adsorption amount; c is the BET constant.	The BET equation is applied to multilayer adsorption scenarios, such as type II and III isotherm curves, depending on the relative scale of adsorbate-adsorbent interaction and adsorbate-adsorbate interaction.

In this work, the type I Langmuir isotherm model is chosen to study the methane adsorption phenomenon in shales for the following two reasons. Firstly, the storage condition for methane in shale reservoirs is usually in high pressure (up to 50 MPa) and high temperature above (273.15 K) regions, in which the methane behaves as a supercritical fluid, and, that is to say, the condensation behavior does not occur; thus, the type IV and type V isotherms do not apply to this case. Secondly, because methane molecules are non-polar, the relative strength of an interaction between the methane molecules and shales is much stronger than an interaction between methane molecules themselves. This leads to methane molecules occupying an adsorbent surface first before layering up onto each other. As shown in Figure 3-2, the values of density of the adsorption layers away from the adsorbent surface decline rapidly as the distance becomes further apart, which suggests that assuming the model of the monolayer for describing the methane adsorption in shales is sufficient enough. These details correspond well to the type I Langmuir monolayer model, and, therefore, it is used in this study. Generally, the type I Langmuir model is widely applied in fitting with actual adsorption data and achieved satisfying results. Additional details of the Langmuir isotherm equation will be discussed in the following sections.

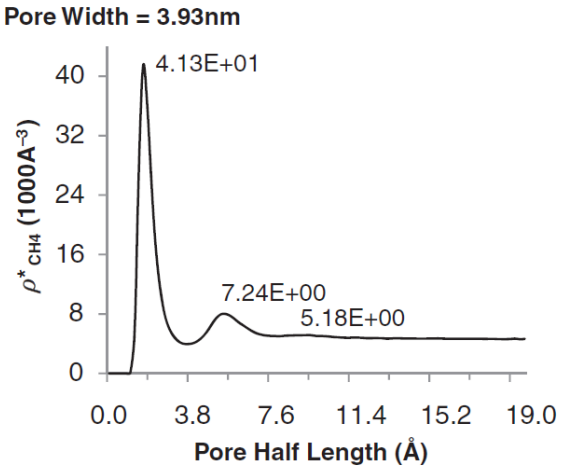

Figure 3-2. Density profile for methane at 176 °F in a 3.93 nm pore (Ambrose et al., 2012)

3.2 Single-site Absolute Adsorption Model

As mentioned in the previous chapter, the absolute adsorption isotherm of methane on shale reservoirs demonstrates the patterns that match closely with the type I Langmuir adsorption model. In fact, when it comes to studying methane gas adsorption phenomenon on various shale rocks compositions (shales, clays, or kerogens), many researchers have chosen to apply the Langmuir monolayer equation for the same reason (Ji et al., 2012; Zhang et al., 2012).

As summarized in Table 3-1 above, the Langmuir monolayer equation for an absolute adsorption amount is a function of n_{max}, P, and P_L, shown in the equation as follows:

$$n_{ab} = n_{max} \frac{P}{P_L + P} \tag{3.1}$$

The value of n_{max}, the maximum adsorption capacity, is with respect to the adsorbed amount at a full capacity of the monolayer. For this value, Langmuir (1918) has indicated that it is independent of both temperature and pressure; rather, it is only related to the actual amount of adsorption sites that are available for the adsorbent. On the other hand, the value of P_L, the Langmuir pressure, depends on the temperature. Specifically, the Langmuir pressure is a function of enthalpy as well as entropy for adsorption (Myers, 2002), as shown as follows:

$$P_L = P^0 \exp\left(-\frac{\Delta S^0}{R}\right) \exp\left(\frac{\Delta H}{RT}\right) \quad (3.2)$$

where P^0 is the pressure at the perfect gas reference state and P^0 equals 0.1 MPa; $\Delta S^0$is the standard molar integral entropy at saturation where the surface energy coverage approaches unity, J/mol/K; ΔH is the differential enthalpy of adsorption, KJ/mol.

As one can see in equation (3.2), the two thermodynamic terms ΔS^0 and ΔH are essential to determine the value of Langmuir pressure. The standard adsorption entropy, ΔS^0, is defined as the change of adsorbate's mobility from the bulk phase to the adsorbed phase (Knox and Dadyburjor, 1981; Xia et al., 2008). When the adsorbate is at the bulk phase, it experiences three-dimensional mobility, which means that its entropy includes the vibrational entropy, translational entropy, as well as the rotational entropy of gas molecules. However, once that adsorbate turns into the adsorbed phase, its entropy loses the contributions from the translational and rotational ones. The only entropy term left for the adsorbate is the vibrational entropy. The reason for this is that once the adsorbate is adsorbed onto the adsorbent, its only movement left is through the two-dimensional vibration. Thus, the term ΔS^0 can also be described by the following equation:

$$\Delta S^0 = S_a^0 - S_g^0 \quad (3.3)$$

where S_a^0 is the entropy of the adsorbate in the adsorbed phase at the state when the adsorbent's surface is fully covered by the adsorbate; S_g^0 is the entropy of the adsorbate in the bulk phase at the atmospheric pressure (Xia et al., 2008). Moreover, the differential enthalpy of adsorption, ΔH, is defined as the difference between the energy required to start the desorption process, E_d,

and the energy required to start the adsorption process (Xia et al., 2016), E_a, as shown as follows:

$$\Delta H = E_d - E_a \tag{3.4}$$

Since the value of ΔH is determined by the activation energy of desorption and adsorption, it reflects the magnitude of an interaction between the adsorbent and adsorbate. When the absolute value of ΔH is relatively large, it means that a larger amount of energy is required to start the desorption process of adsorbate from the adsorbent, which also corresponds to the fact that only a less amount of activation energy is needed for the adsorption process to begin.

In order to take a closer look at the relationship between the adsorption entropy and enthalpy, a review of this data has been conducted and an almost linear relationship is suggested to represent the value of ΔS^0 and the value of ΔH. This data is from both experimental and simulation results that have been collected by other researchers from the sources of shale, kerogen, and coal, after combining them all together, and Figure 3-3 is generated:

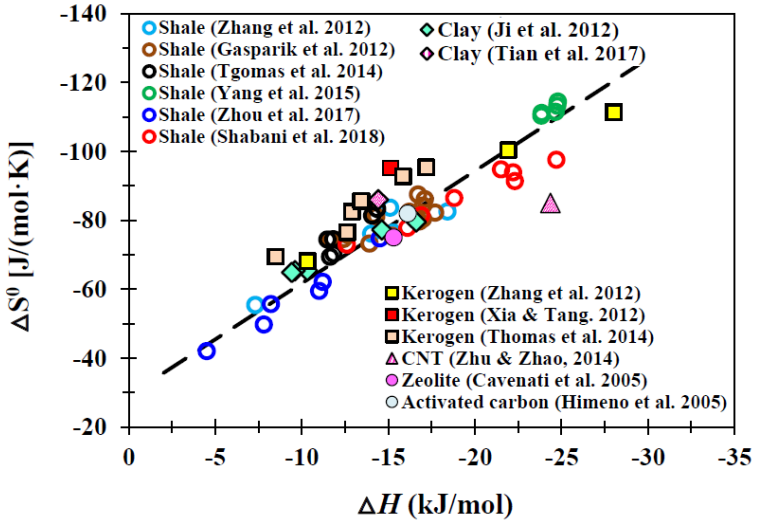

Figure 3-3. A linear relationship between adsorption entropy and enthalpy (Li et al., 2018)

To validate this linear relationship between ΔS^0 and ΔH suggested by Figure 3-3, equation (3.3) is looked at again for additional details. As explained earlier, the value of S_g^0 can be taken as a constant value as it represents the entropy of the adsorbate in the bulk phase at the atmospheric pressure. Thus, the value of ΔS^0 is directly determined by the value of the term S_a^0. The larger the value of S_a^0 is, the less restriction there is for the adsorbate from the adsorbent. That phenomenon reflects a weak strength of the interaction between the adsorbate and the adsorbent, which, in turn, reflects a smaller value of the adsorption enthalpy, ΔH. This theoretical explanation corresponds well to the linear relationship of ΔS^0 and ΔH shown in Figure 3-3.

3.3 Multi-site Absolute Adsorption Model

Even though the Langmuir absolute adsorption model has demonstrated positive results with studying the methane adsorption in shale reservoirs, it does have one shortcoming with this model, which is associated with the nature of the shale reservoirs. As mentioned in Section 3.2, this Langmuir adsorption model has been widely used to investigate the adsorption behaviors of each of the shale rock compositions individually. In reality, shale rocks are often made of a variety of compositions, such as shale, clay, and kerogen. The Langmuir model, however, is based on the assumption that the adsorbent is a homogeneous surface (Langmuir, 1918). Therefore, it is inappropriate to apply this Langmuir single site homogeneous model directly to heterogeneous shale rocks when it comes to studying the real methane adsorption behaviors.

3.3.1 Heterogeneity of shale.

Since shale rocks are often made up of several different compositions, their adsorption energy is usually heterogeneous as well across their surfaces, meaning that various adsorption energy is observed on their surfaces instead of a singular value for an entire adsorbent. To

understand the characteristics of energy heterogeneous surfaces of shale rocks, first it is critical to understand the methane adsorption energy characteristics for each composition of a shale reservoir.

As shown in Figure 3-4, the methane adsorption heat for clay lies in the range between 9.6 KJ/mol and 16.6 KJ/mol, which means that various clays have various capabilities towards methane adsorption. Meanwhile, when it comes to methane adsorption on isolated kerogens, their heat of adsorption is in a much wider range, from 8.46 KJ/mol to 21.9 KJ/mol. This observation indicates that methane adsorption on kerogens is rather a complicated issue; in fact, this wide range of adsorption heat is due to the various types of kerogens as well as different stages of their thermal maturity. The type of kerogen that has a more proportion of hydrophobic aromatic hydrocarbon groups relative to hydrophilic aliphatic groups is likely to show a higher value of methane adsorption heat due to the preference of methane to be attracted by the hydrophobic materials (Zhang et al., 2012; Hu et al., 2014; Hu et al., 2015). The various stages of thermal maturity of kerogen affect its value of methane adsorption heat similarly. As the thermal maturity increases, the proportion of hydrophobic aromatic hydrocarbon groups relative to hydrophilic aliphatic groups starts to increase as well due to the continual removal of hydrophilic aliphatic groups. Thus, a higher value of methane adsorption heat is achieved as the kerogen becomes more matured (Gasparik et al., 2014; Yang et al., 2017; Huang et al., 2018).

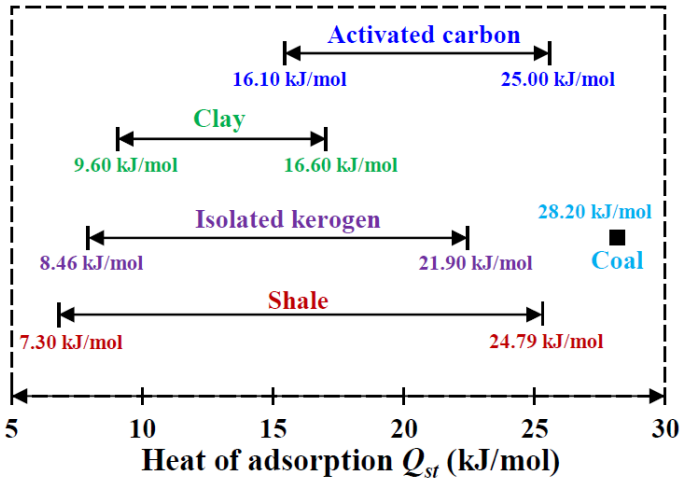

Figure 3-4. The heat of adsorption for various materials (Li et al., 2018)

Other than the effect of composition mentioned earlier, a pore size of adsorbents also affects their adsorption energy. In the case with a smaller pore size, the interaction between a fluid and a wall is stronger than that in the case of a larger pore size. Therefore, a smaller pore size leads to higher adsorption energy (Blanco et al., 2016; Xiong et al., 2017). As one can see from Figure 3-5, for various materials of adsorbents, as the pore size decreases, their average isosteric heat (adsorption energy) increases. When the pore size is smaller than 10 nm, as the pore size becomes smaller, the change in the adsorption energy is significantly large. On the contrary, in the case where a pore size is greater than 10 nm, as the pore size increases, the change in adsorption energy is noticeably less. As one can see in this case for quartz, once the pore size passes the mark of 10 nm, its adsorption energy stays somewhat unchanged. In the case of C4, as its pore size increases from 2 nm to 20 nm, its adsorption energy decreased almost as twice from 16 KJ/mol to 8 JK/mol.

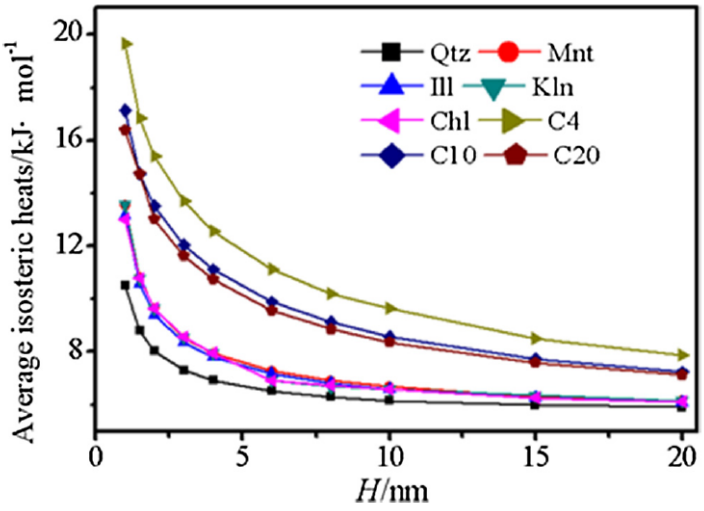

Figure 3-5. The average isosteric heat of adsorption of the methane of in the pores of different sizes (Xiong et al., 2017)

3.3.2 Multi-site adsorption.

Since compositions and pore sizes play critical roles in determining the adsorption energy, merely assuming a homogeneous surface with constant adsorption energy is not applicable any longer to analyze the complex methane adsorption on strongly heterogeneous shales. To overcome this challenge, a new model is required to address a variety of shale rocks compositions, as well as pore size distributions, i.e., multiple adsorption sites across adsorption surfaces; thus, the following equations are provided for such a purpose:

$$n_{ab} = n_{max} \sum_{i=1}^{i=n} \alpha_{(i)} \frac{P}{P_{L(i)}+P} \tag{3.5 a}$$

$$P_{L(i)} = P^0 \exp(-\frac{\Delta S^0_{(i)}}{R}) \exp(-\frac{Q_{st(i)}}{RT}) \tag{3.5 b}$$

where n is the number of the adsorption sites that are available; $\alpha_{(i)}$ is the fraction of a single adsorption site; $P_{L(i)}$ is the Langmuir pressure for a single adsorption site, MPa; $\Delta S^0_{(i)}$ is the

standard entropy for a single adsorption site, J/mol/K; $Q_{st(i)}$ is the adsorption heat for a single adsorption site, KJ/mol.

Compared with the single site Langmuir adsorption model, this model embraces the intricate compositions of natural shale rocks and is, therefore, more valid to be applied to analyze the real methane gas adsorption behaviors. Nevertheless, this model contains more unknown variables compared with the single site Langmuir model. Specifically, the unknown parameters in the equations include: n_{max}, $\alpha_{(i)}$, $\Delta S^0_{(i)}$, and $Q_{st(i)}$. In order to simplify the model and make it more applicable to use, two simplifications are made in this thesis:

(1) Taking an average value of entropy for adsorption to eliminate the parameter $\Delta S^0_{(i)}$. Generally, this practice is common as an identical value of the average entropy since adsorption is often employed in many adsorption cases (Xia et al., 2006). Thus, equation (3.5 b) becomes:

$$P_{L(i)} = P^0 \exp(-\frac{\Delta S^0_m}{R}) \exp(-\frac{Q_{st(i)}}{RT}) \tag{3.6}$$

where ΔS^0_m is the average or apparent standard entropy for adsorption, J/mol/k.

(2) Assuming a Gaussian distribution is often the case with the adsorption heat $Q_{st(i)}$ for shales, as described by equations (3.7 a, b, c, d) below:

$$f_{(i)} = \frac{1}{\sigma\sqrt{2\pi}} \exp(-\frac{(Q_{st}-Q_m)^2}{2\sigma^2}) \tag{3.7 a}$$

$$f_T = \int_{Q_{min}}^{Q_{max}} \frac{1}{\sigma\sqrt{2\pi}} \exp(-\frac{(Q_{st}-Q_m)^2}{2\sigma^2}) dQ_{st} \tag{3.7 b}$$

$$\alpha_{(i)} = \frac{f_{(i)}}{f_T} \tag{3.7 c}$$

$$\sum_{i=1}^{i=n} \alpha_{(i)} = 1 \tag{3.7 d}$$

where Q_m is the mean value for the adsorption heat of the adsorbent, KJ/mol; σ is the standard deviation of the normal distribution. Instead of having negative infinity and positive infinity as the lower and upper limit for adsorption heat, values of 0 KJ/mol and 30 KJ/mol are assumed, respectively. These two values are chosen to agree with the adsorption heat values observed for various shales compositions shown in Figure 3-4. Based on these two values of limitations, three scenarios with low energy, middle energy, and high energy dominated surfaces are shown in Figure 3-6.

Through these two simplifications above, the number of unknown parameters in this multi-site Langmuir model is eliminated from 3n+1 to only 4 left, which are n_{max}, ΔS_m^0, Q_m, as well as σ. Now, compared with the single site Langmuir model, this simplified multi-site model only has one additional unknown parameter.

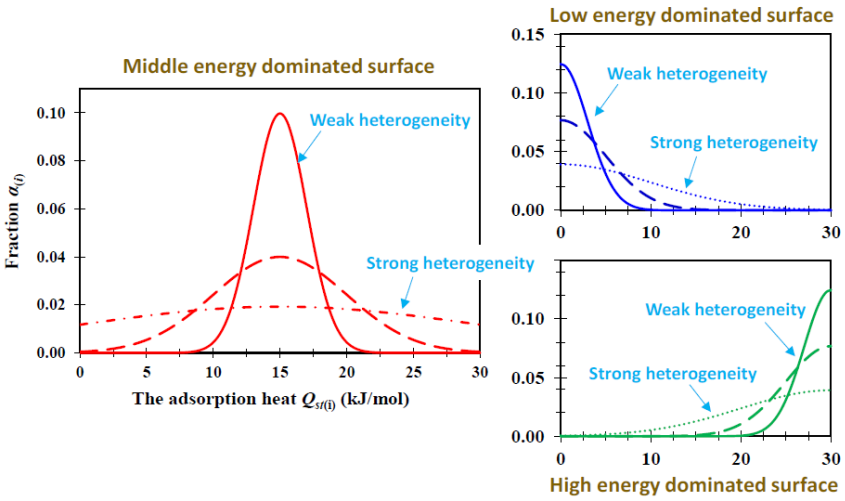

Figure 3-6. Three scenarios with low energy, middle energy, and high energy dominated surface (Li et al., 2018)

3.4 Excess Adsorption Model

As discussed in Chapter 2, the equation of excess adsorption is closely related to that of the absolute adsorption. Their only difference is characterized by the bulk gas phase volume that

takes up the adsorbed phase volume in the absolute adsorption. Therefore, similarly to the absolute adsorption model, there are derived models available to describe the phenomenon of excess adsorption. The excess adsorption models depict the adsorption behaviors that take place during the measured adsorption experiments as shown in Figure 2-6.

3.4.1 Single-site excess adsorption model.

When shale rocks' heterogeneity is not considered, the single site excess adsorption model is applicable to describe the measured adsorption process on an assumed homogeneous surface. This model is obtained by substituting both equation (3.1) for single site absolute adsorption and equation (2.5) for the adsorbed phase density into equation (2.3), and the following equation is generated:

$$n_{ex} = n_{max} \frac{P}{P_L + P} \left(1 - \frac{\rho_g}{\rho_l} e^{\lambda(T - T_b)}\right) \tag{3.8}$$

The parameters listed in this equation are the same as appearing in the original equation. The value of ρ_g is calculated using the RK EOS equation discussed in Section 2.2 in Chapter 2. Despite its successful application of fitting the measured experimental adsorption data, this model cannot address the heterogeneity of actual shale rock surfaces. Therefore, a multi-site model is also required to accurately depict the excess adsorption behaviors.

3.4.2 Multi-site excess adsorption model.

Similarly, just like the single site excess adsorption equation, the multi-site excess adsorption model can also be derived by substituting both equation (3.5 a) of the multi-site absolute adsorption model and equation (2.5) of the adsorbed phase density into equation (2.3), the result is shown as the following equation below:

$$n_{ex} = n_{max} \sum_{i=1}^{i=n} \alpha_{(i)} \frac{P}{P_{L(i)} + P} \cdot \left(1 - \frac{\rho_g}{\rho_l} e^{\lambda(T - T_b)}\right) \tag{3.9 a}$$

$$P_{L(i)} = P^0 \exp(-\frac{\Delta S^0_{(i)}}{R}) \exp(-\frac{Q_{st(i)}}{RT}) \quad (3.9\ b)$$

To simplify this model, the same simplifications used for the multi-site absolute adsorption model for parameters $P_{L(i)}$ and $\alpha_{(i)}$ are applied to this model as well.

In the next chapter, the Langmuir monolayer model and the multi-site adsorption model will be applied to fit the experimentally measured adsorption data for both absolute adsorption and excess adsorption models for comparison.

3.5 Summary

In this chapter, both the absolute adsorption models and excess adsorption models are presented and discussed in detail concerning their equations derivation, parameters explanation, as well as the physical meaning behind each model. In summary, the following conclusions can be drawn:

- Generally, six types of adsorption isotherms are available to describe the adsorption behaviors according to the IUPAC classification. The type I isotherm is selected for this work to characterize the methane adsorption behaviors in shales. This is due to a non-condensation nature for supercritical methane at its storage condition in most shale reservoirs and a relatively strong interaction between methane molecules and adsorbent, which leads to an excellent fitting with experimental adsorption data.
- The traditional single site Langmuir adsorption model is commonly applied to investigate the methane adsorption in shales. However, this model assumes that a surface is homogeneous, and thus it is incapable to address the heterogeneity (various mineral materials and pore sizes) of shales on methane adsorption. Therefore, in order

to accurately analyze the methane adsorption behaviors on shales, an adsorption model with an assumption of a heterogeneous surface is needed.

- A multi-site adsorption model is built by taking the effect of heterogeneous energy on the methane adsorption behavior into consideration, which is a function of $\Delta S^0_{(i)}$, $\alpha_{(i)}$, and $Q_{st(i)}$. To simplify this model, two fundamental assumptions are made, one is to assume a constant value of $\Delta S^0_{(i)}$, and the other one assumes that the relationship of $\alpha_{(i)}$ and $Q_{st(i)}$ follows the Gaussian distribution. The second assumption makes it possible to analyze the low, middle, and high adsorption energy dominated surfaces.

Chapter 4: Adsorption Experiments and Isotherms Analysis

4.1 Materials and Experiments

In this chapter, a series of methane adsorption experiments are conducted with actual shales samples collected from China, and the measured adsorption isotherms are validated with the adsorption models introduced in Chapter 3. The following two sub-sections will introduce the characteristics of the four shale samples as well as the setup of the experiments for the methane adsorption isotherm.

4.1.1 Shale samples characteristics.

In order to find out the mineralogical characteristics of these shale samples used in this study, the methods of X-ray diffraction analysis (XRD) is done; to find the characteristics of the organic matter in these samples, total organic carbon (TOC) and rock-eval analysis, as well as vitrinite reflectance have been carried out prior to the methane adsorption experiments.

The XRD is carried out on the four shale samples S1 to S4 to find out their bulk mineralogical compositions. The four samples are first crushed and milled to powders with an average particle size of 100 mesh. Then the device called a Bruker D8 discover diffractometer is used to scan those random orientated samples from 5^0 to 60^0 2θ. The results obtained from XRD analysis are shown in Table 4-1. As one can see, bulk mineralogical compositions of these four shale samples are similar. The content of quartz is one of the primary compositions of these shales (31-48%). Other than quartz, the total clay content also contributes significantly to the overall bulk compositions (15-38%). Out of the clay compositions, the dominant one is illite (69-88%).

Table 4-1. Shale samples mineralogical compositions (Li et al., 2018)

Sample	Quartz	Feldspar	Calcite	Dolomite	Pyrite	Anhydrite	Total Clay	Clay Composition (%)				
								S	I/S	I	K	C
S-1	38	20	4	7	4	2	25	/	19	81	/	/
S-2	31	17	2	6	5	1	38	/	24	69	/	7
S-3	48	12	12	9	3	1	15	/	10	88	2	/
S-4	43	11	3	15	4	/	24	/	13	86	/	1

S: Smectite; I/S: Illite-Smectite mixed layer; I: Illite; K: Kaolinite; C: Chlorite; TOC: Total Organic Carbon.

The TOC determination is done by the device called a Leco CS-230 carbon/sulfur analyzer. Again, the four samples are crushed and milled to powder with an average particle size of 100 mesh, then heated to 550 ^{0} C. The results of TOC for the four samples are shown in Table 4-2. Their TOC values range between 2.13 and 4.48 wt%. The Rock-Eval analysis is conducted on the four shales samples as well to find out the type of the organic matter and its maturity, as well as its potential for hydrocarbon generation. The rock-eval analysis is carried out with the Delsi Rock-Eval OSA pyrolysis instrument to measure the parameters S1, S2, S3, and T_{max}. S1 is the indication of the amount of free hydrocarbons that exist in the sample. S2 is the number of nonvolatile hydrocarbons, and S3 is the amount of the oxygen contained organic compounds that are released through thermal cracking of the organic matter in the samples. The value of T_{max} is the temperature at which the S2 value is of its maximum. This value shows the thermal maturity of the samples. The results for these values are shown in Table 4-2 as well.

Other than using the value of T_{max} as the thermal maturity indicator, we have also applied the method of vitrinite reflectance (R_o) to measure the samples' thermal maturity. For each shale sample, various points are selected to measure its bituminite reflectance first. Then we convert those values to the vitrinite reflectance with the formula proposed by Jacob (1989). The calculated values are listed in Table 4-2. As one can see, the relative magnitudes of those values are corresponding to the magnitudes of the value of T_{max}.

Table 4-2. Shale samples total organic content (TOC) (Li et al., 2018)

Sample	TOC (wt%)	Type	Ro(%)	S1(mg/g)	S2(mg/g)	S3(mg/g)	IH(S2/TOC)	IO(S3/TOC)	Tmax(°C)
S-1	2.13	II	2.06	1.5	2	0.6	93.9	28.2	507
S-2	2.56	II	1.97	1.8	2.1	0.5	82	19.5	502
S-3	3.37	II	1.86	2.7	3.7	0.7	109.8	20.8	496
S-4	4.48	II	1.78	3.9	4.2	1.1	93.8	24.6	491

S1: the amount of free hydrocarbon; S2: the number of hydrocarbons generated from thermal cracking; S3: the amount of carbon dioxide released; T_{max}: temperature for the maximum release of hydrocarbon; I_H: hydrogen index; I_o: oxygen index.

In addition to the investigation of shale samples' compositions and organic characteristics, we have also investigated other physical properties of these samples, such as the grain density, bulk density, total pore volume and total porosity by the helium porosimetry method. The helium porosimetry method is an accurate method to determine shale densities and pore volumes due to the capability of helium gas entering small pores of shale samples. The results obtained are listed in Table 4-3. Both the grain density and bulk density values are comparable for four samples. The value of the total pore volume is in the same trend as the total porosity.

Table 4-3. Shale samples physical characteristics (Li et al., 2018)

Sample	Grain Density (g/cm^3)	Bulk Density (g/cm^3)	Total Pore Volume (cm^3/g)	Total Porosity (%)
S-1	2.25	2.49	0.0141	3.5
S-2	2.30	2.21	0.0186	4.1
S-3	2.56	2.43	0.0210	5.1
S-4	2.74	2.49	0.0365	9.1

4.1.2 Methane adsorption experiments.

Once the previous analyses are finished, the four shale samples are then crushed and milled to about 100 mesh with average particle sizes of 150 μm. Then those powders are put into an oven at 110 °C for 24 hrs to dry up. Once that is completed, the methane adsorption isotherm experiments are ready to start.

Our experiments are conducted by a volumetric method with the help of equipment called an IMI isotherm analyzer (manufactured by Hiden Analytical Ltd. in England), as shown in

Figure 4-1. This equipment is a highly automatic one, and its main procedures are controlled by an embedded computer in the Process Control Interface (PCI), including the free volume measurement, pressure recording, and uptake recording. There are two steps we take to do this experiment with this equipment. The first step is to add the weighted sample inside the sample cell and the second step is to set the equilibrium pressure and the temperature. In this study, we conduct the experiments at three different temperatures, which are 30 °C (303.15 K), 60 °C (333.15 K) and 90 °C (363.15 K). The pressure range for this experiment is between 0.5 MPa and 20 MPa. The temperature and pressure ranges are set this way to mimic the actual shale reservoir conditions. For each sample, we collect 16 data of methane uptake versus pressure at three temperature conditions.

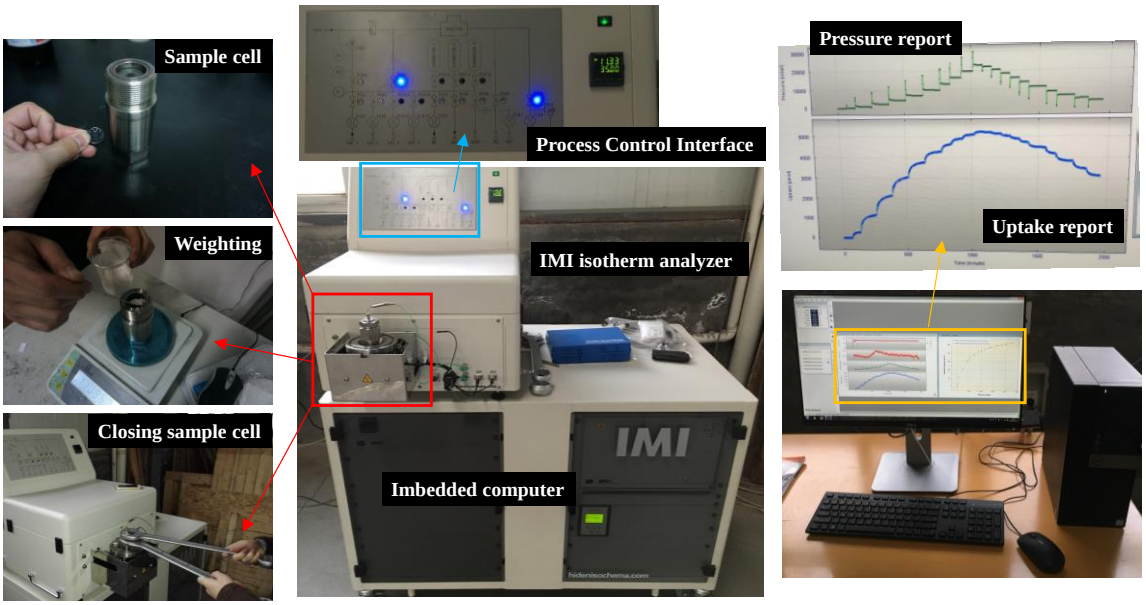

Figure 4-1. Volumetric adsorption method experimental set-up

4.2 Adsorption Isotherms Fitting with Experiments Data

Once the above adsorption experiments are done and the required data is collected, we then start to apply the excess adsorption models (both the single-site and multi-site equations)

that we derived earlier in Chapter 3 to fit with the measurement data to check if these two models are valid to represent the real adsorption scenarios.

4.2.1 Single-site excess adsorption model.

As shown in equation (3.8), the single-site excess adsorption model has three parameters that we can potentially be modified to fit the calculated adsorption values with the measured data. These three parameters are n_{max}, P_L, and λ. After trials and errors with modifying these three parameters, our calculated results are well fitted with the measured adsorption data for our four shale samples with temperature ranging from 303.15K to 363.15 K and pressure up to 20 MPa, as shown in Figure 4-2. The fitting parameters are summarized in Table 4-4.

As one can see from values of these three parameters, for each sample shale, the values of n_{max} and λ are the same regardless of the temperature changes. The value of n_{max} is a property of the adsorbent and only related to the number of the adsorption sites available to the adsorbent; therefore, the temperature has no effect on it. The value of λ is a property of the adsorption fluid, which is methane in our case and this value is also not affected by the temperature either. The only parameter that fluctuates with the temperature is P_L. The reason behind this can be explained by equation (3.2), which shows that P_L is a function of temperature and two thermodynamic parameters ΔS^0 (adsorption entropy) and ΔH (adsorption enthalpy). To find out the values of these two parameters for each shale sample, a linear relationship between P_L and these two parameters is derived from equation (3.2) as follows:

$$\ln P_L = \frac{\Delta H}{RT} - \frac{\Delta S^0}{R} + \ln P^0 \tag{4.1}$$

Since we already have the values of P_L, R, T, and P^0, the two unknown values of $\Delta S^0$and ΔH of each sample can be calculated from the intercept and slope of the linear relationship between

$\ln P_L$ and $\frac{1}{T}$, as demonstrated in Figure 4-3. The calculated values of ΔS^0 and ΔH for these four samples are summarized in Table 4-4 as well. As one can see, sample S-4 has the largest absolute values of adsorption enthalpy and entropy compared to the rest of the samples. That means the binding energy for methane molecules on S-4 is significantly higher compared to that of the rest samples.

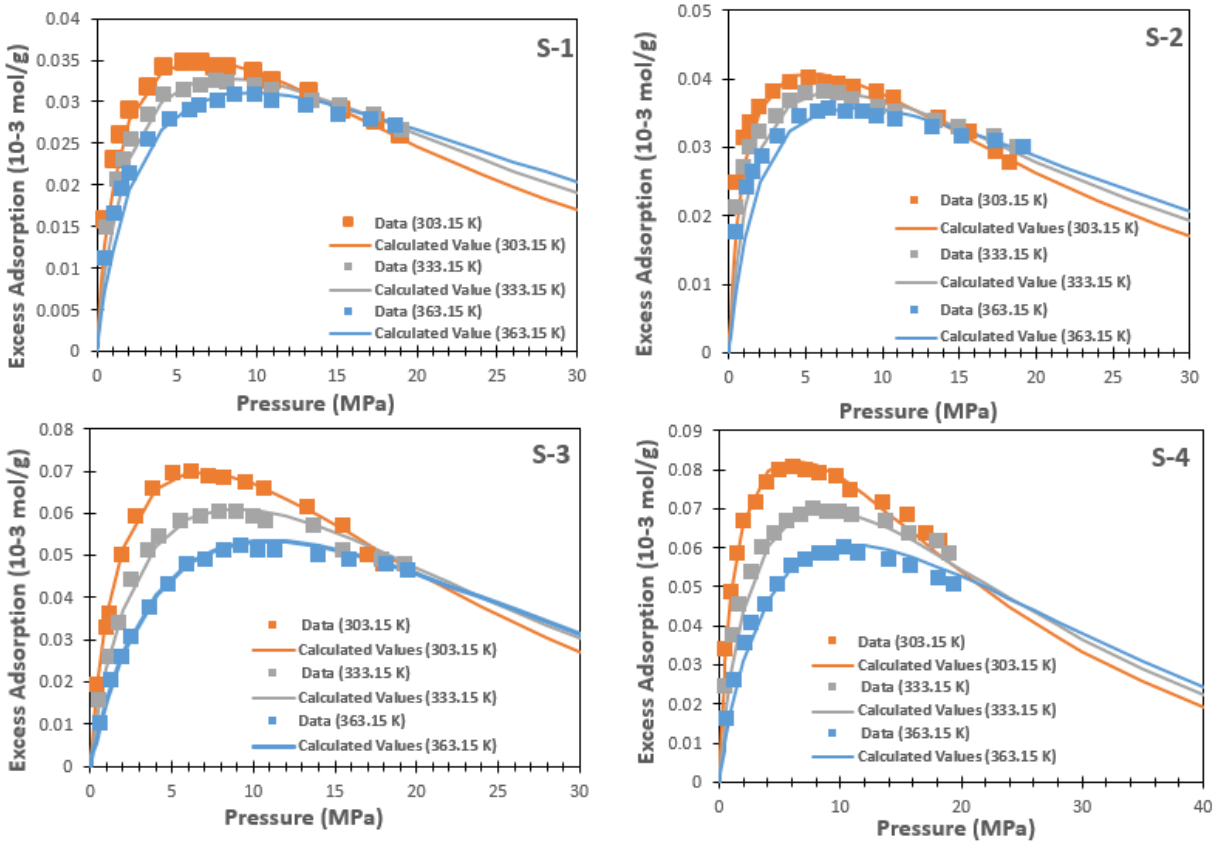

Figure 4-2. Fitting results of experimental adsorption data with single-site excess adsorption model at 303. 15 K, 333.15 K, and 363.15 K for four shale samples (Li et al., 2018)

Table 4-4. Fitting parameters of single-site excess adsorption model (Li et al., 2018)

Sample	Temperature T (K)	Maximum Adsorption n_{max} (10^{-3} mol/g)	Langmuir Pressure P_L (MPa)	Expansion Coefficient λ (k^{-1})	Standard Entropy ΔS^0(J/mol/K)	Enthalpy ΔH (KJ/mol)
S-1	303.15	0.05	1.45	0.0015	-58.01	-10.84
	333.15		2.15			
	363.15		2.95			
S-2	303.15	0.055	0.95	0.0018	-62.21	-13.17
	333.15		1.55			
	363.15		2.25			
S-3	303.15	0.11	2.05	0.0022	-77.91	-16.00

	333.15		3.65			
	363.15		5.85			
S-4	303.15	0.12	1.45	0.002	-89.33	-20.27
	333.15		3.25			
	363.15		5.45			

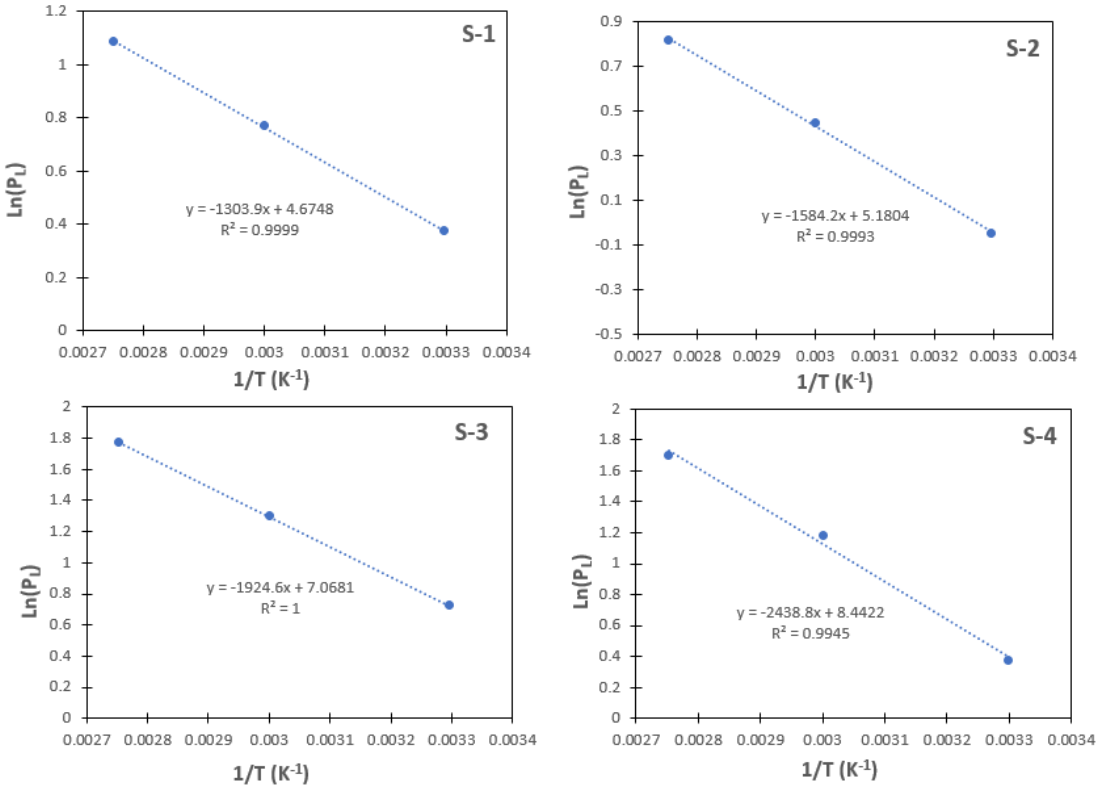

Figure 4-3. A linear relationship between ln P_L and $\frac{1}{T}$ for four shale samples (Li et al., 2018)

4.2.2 Multi-site excess adsorption model.

As shown in equations (3.6), (3.7), and (3.9), the multi-site excess adsorption model has five parameters that we can potentially modify to fit the calculated adsorption values with the actually measured data. These five parameters are n_{max}, ΔS_m^0, Q_m, σ, and λ. After trials and errors with modifying these five parameters, our calculated results are well fitted with the measured adsorption data for our four shale samples with temperature ranging from 303.15K to 363.15 K and pressure up to 20 MPa, as shown in Figure 4-4. The fitting parameters are summarized in Table 4-5. As one can see, all the parameters listed in this table are independent of the effect of temperature.

The energy distribution of each sample is also illustrated in Figure 4-5 with a comparison of the constant adsorption value of the single-site adsorption model. As one can see in these figures, the multi-site adsorption model for each sample has a wide range of values for adsorption energy due to the consideration of heterogeneity. On the contrary, the single-site adsorption model is incapable of addressing the various adsorption energy across the shale surface. It assumes a constant value for adsorption energy instead. Because of that, the single-site model lacks physical meaning when it comes to describing the adsorption heat distribution across the shale surfaces. More comparisons of these two models, regarding their accuracy against the measured experimental data, will be made in the following section.

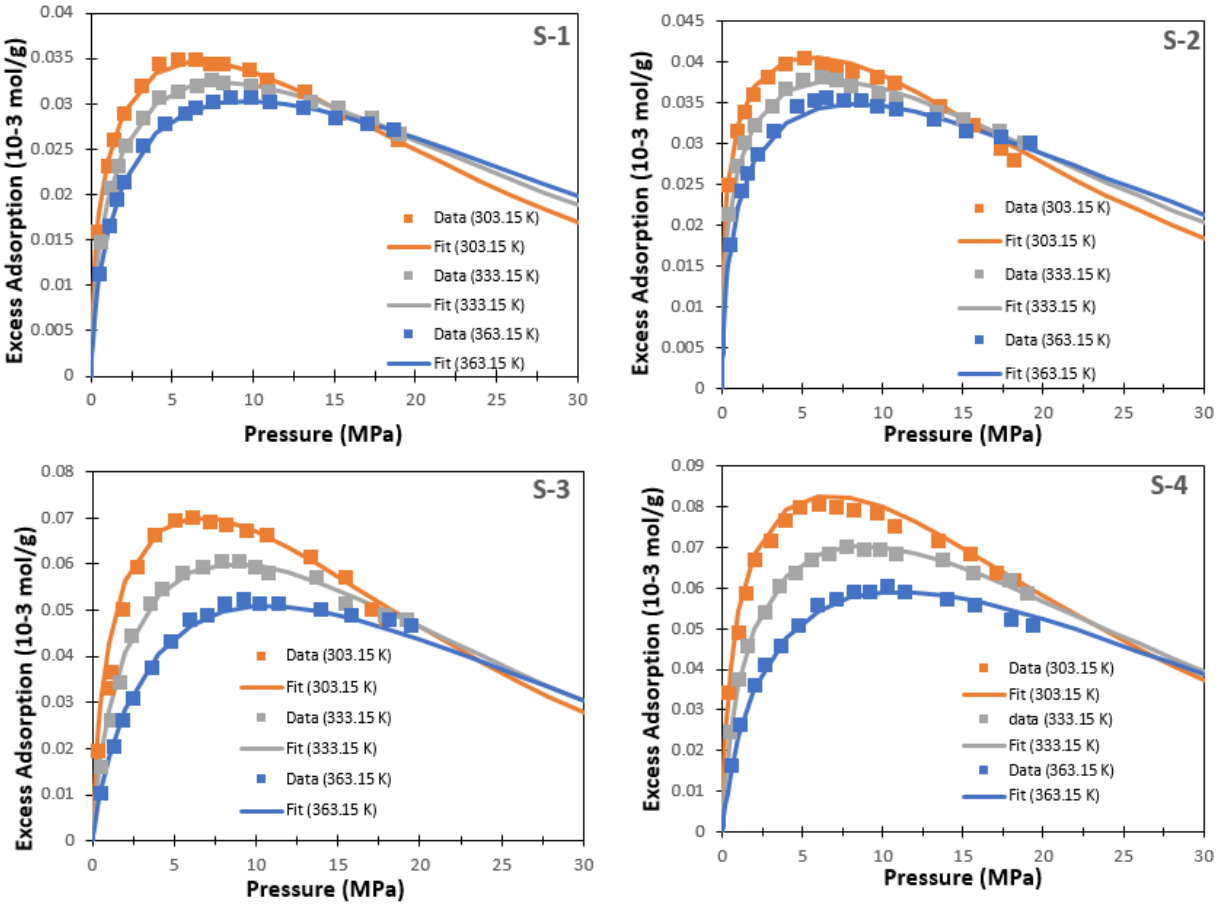

Figure 4-4. Fitting results of experimental adsorption data with multi-site excess adsorption model at 303. 15 K, 333.15 K, and 363.15 K for four shale samples (Li et al., 2018)

Table 4-5. Fitting parameters of multi-site excess adsorption model (Li et al., 2018)

Sample	Maximum Adsorption n_{max} (10^{-3} mol/g)	Standard Entropy ΔS_m^0(J/mol/K)	Adsorption Heat (mean) Q_m (KJ/mol)	Standard Deviation σ (dimensionless)	Expansion Coefficient λ (k^{-1})
S-1	0.06	-66	-12.5	5	0.0017
S-2	0.07	-76	-17	8	0.0018
S-3	0.116	-90.5	-20	3	0.0022
S-4	0.16	-98	-22	6	0.002

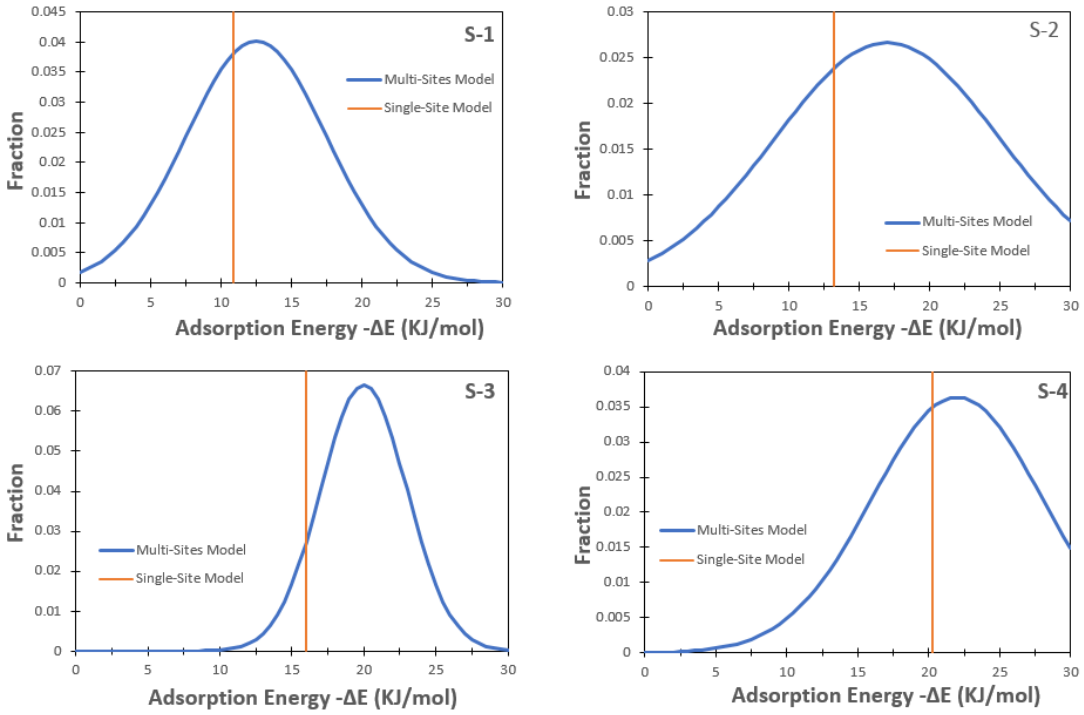

Figure 4-5. Comparison of multi-site adsorption model's energy distribution with the single-site adsorption model's constant adsorption value for each shale sample

4.2.3 Comparison of two models.

As shown in the previous two sub-sections, both the single-site model and multi-site model have achieved acceptable fitting results with the experimentally measured data. Now, it is time to compare these two models regarding their accuracy with this data.

Figure 4-6 demonstrates the comparison of these two models for the four samples and Table 4-6 is generated to summarize the percentage of errors of applying each model for each sample. As one can see in this table as well as the histogram in Figure 4-7, the results calculated by the multi-site model have a lower percentage of errors compared with those of the single-site

model for all four samples. The multi-site adsorption model predicts better adsorption behaviors of methane on shales because it addresses the heterogeneity of shales surfaces by having a wide range of adsorption heat values instead of having a constant value, which is the case for the single-site model.

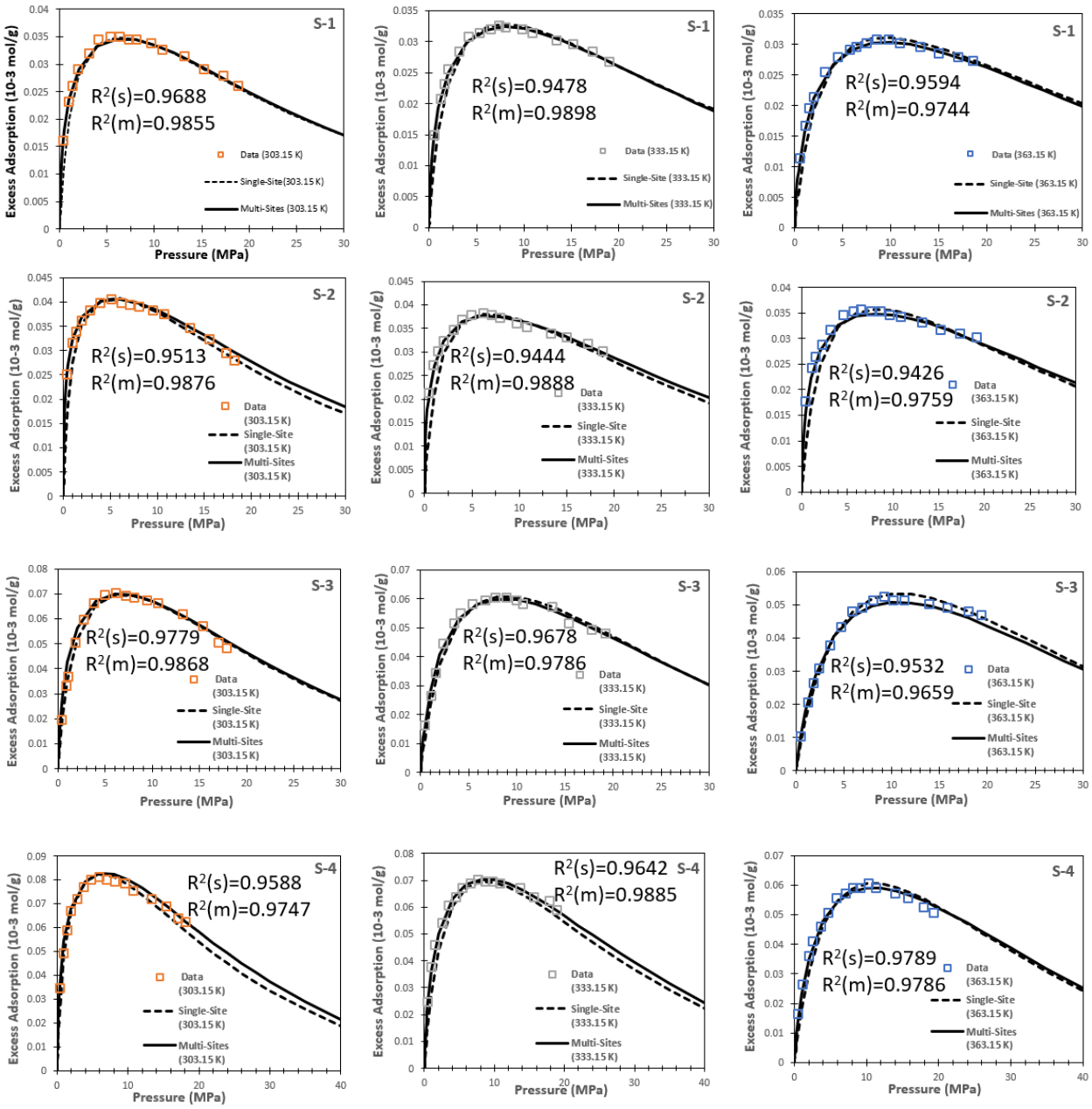

Figure 4-6. Comparison of single-site and multi-site excess adsorption model for the four samples at 303.15 K, 333.15 K, and 363.15 K (Li et al., 2018)

Table 4-6. Comparison of single-site and multi-site excess adsorption model with measured data

Sample	Temperature (K)	Percentage of Error (%)	
		Single-Site Model	Multi-site Model
S-1	303.15	3.12	1.45
	333.15	5.22	1.02
	363.15	4.06	2.56
S-2	303.15	4.87	1.24
	333.15	5.56	1.12
	363.15	5.74	2.41
S-3	303.15	2.21	1.32
	333.15	3.22	2.14
	363.15	4.68	3.41
S-4	303.15	4.12	2.53
	333.15	3.58	1.15
	363.15	2.11	2.14

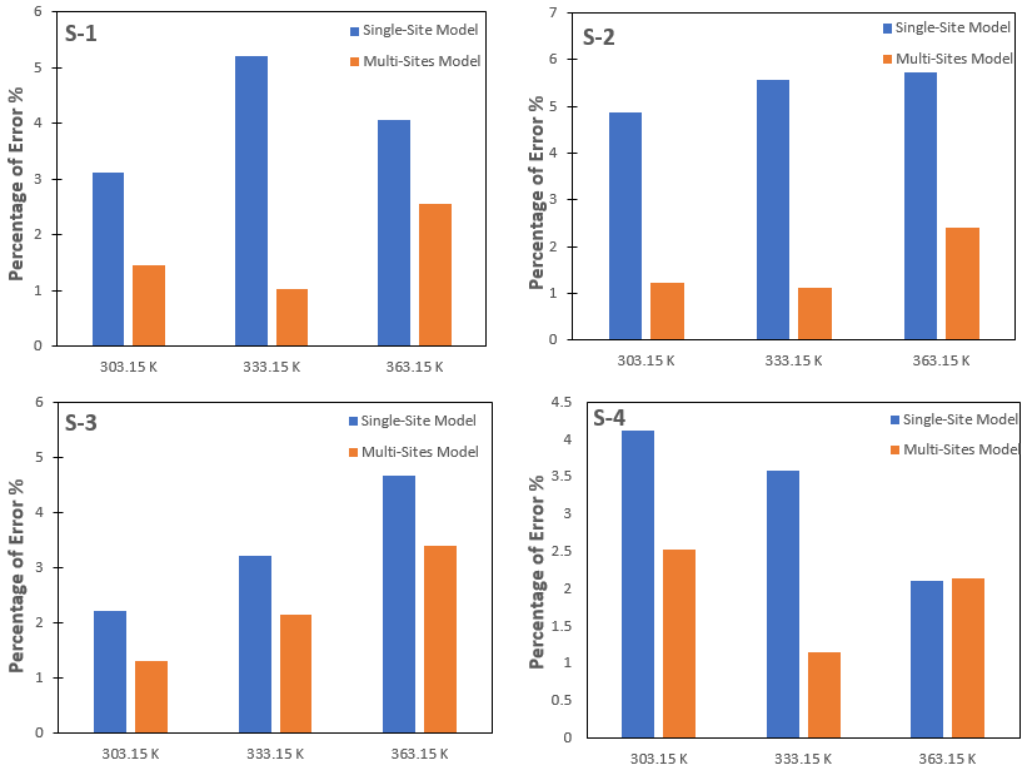

Figure 4-7. Histogram of percentage of error for single-site and multi-site adsorption model with measure data

4.3 Absolute Adsorption and Excess Adsorption

In the previous sections, we have compared the single-site and multi-site adsorption models with the actual experimental data and concluded that the multi-site model is more accurate when it comes to predicting the methane adsorption behaviors on shales. In this section,

we will compare the absolute adsorption and excess adsorption isotherms of the multi-site model. To compare these two isotherms, first, we need to use the parameters listed in Table 4-5 and substitute them into equation (3.5) to obtain the absolute adsorption isotherm for each sample under three different temperatures. Then we plot them together with the excess adsorption isotherms under the same conditions, as shown in Figure 4-8.

As one can see in those curves, the absolute adsorption always decreases while the temperature increases. The excess adsorption isotherm curves have similar behaviors with those of the absolute adsorption isotherm curves up to a particular pressure. Then there comes a change, when the temperature goes higher and the adsorption uptake becomes less. This change is observed with the crossovers of the excess adsorption isotherm curves under three different temperatures in Figure 4-8. The effect of temperature on absolute adsorption is well understood and can be attributed to the thermodynamic theory, which states that as the temperature increases, the gas molecules become more kinetic and, therefore, the residence time on the shale rocks becomes significantly shorter. Because of that, an apparent reduction in the absolute adsorption occurs (Do, 1998).

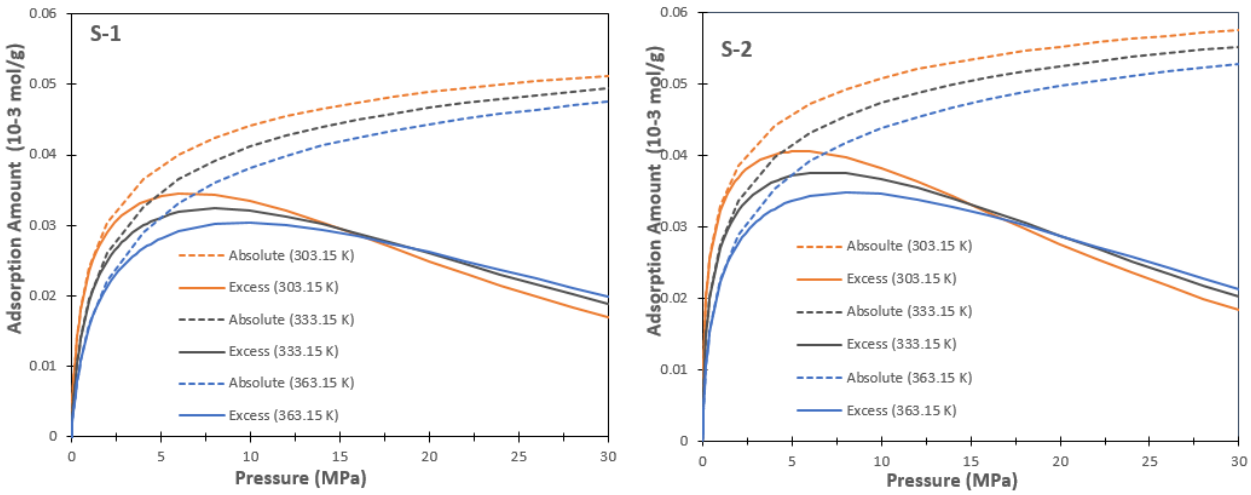

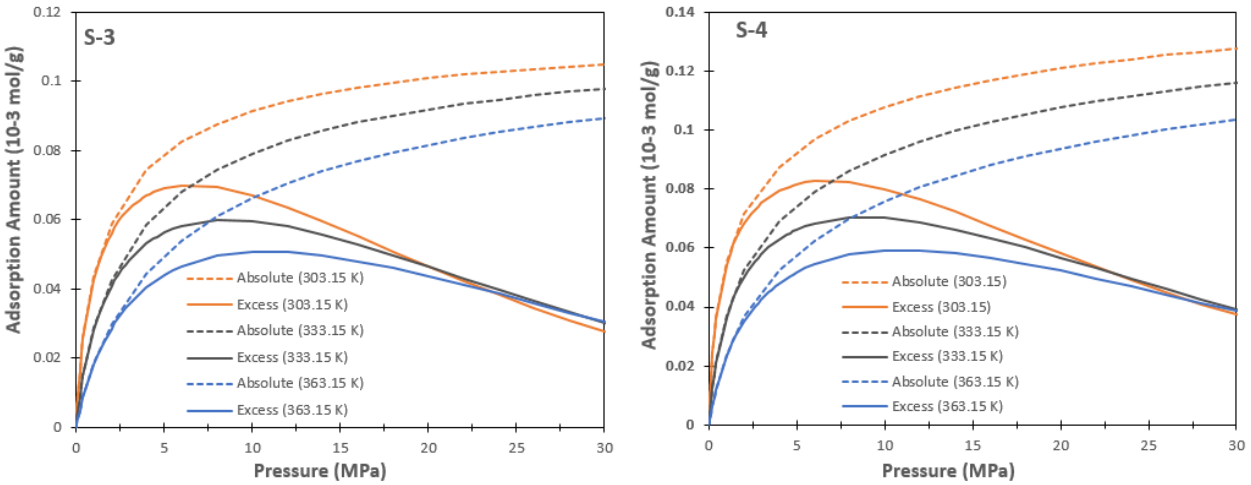

Figure 4-8. Comparison of absolute adsorption and excess adsorption isotherms (Li et al., 2018)

Compared with the straightforward effect of temperature on absolute adsorption, the effect of temperature on excess adsorption is instead a complex issue and needs to be studied in detail. As equation (2.3) shows, the uptake amount of methane depends on the relative magnitude of n_{ab} and $(1-\frac{\rho_g}{\rho_a})$. As discussed above, when temperature increases, the absolute adsorption value of n_{ab} decreases. On the other hand, the value of $\left(1-\frac{\rho_g}{\rho_a}\right)$ starts to increase, which is due to the fact that the value of ρ_g starts to decrease as temperature increases. Since these two values are in inverse trends with the effect of temperature, whether the value of the excess adsorption increases or decreases depends on the relative magnitudes of these two terms.

To find out more about the relative magnitudes of n_{ab} and $\left(1-\frac{\rho_g}{\rho_a}\right)$, a couple of curves are generated in Figure 4-9 to show the effect of temperature on the values of $\frac{n_{ab}}{n_{max}}$ and $\left(1-\frac{\rho_g}{\rho_a}\right)$ under both high and low pressure conditions. As one can see in Figure 4-9-a, in low pressure conditions (5 MPa), the value of $\left(1-\frac{\rho_g}{\rho_a}\right)$ does not change much as the temperature increases from 300 K to 400 K. Under such conditions, $\left(1-\frac{\rho_g}{\rho_a}\right)$ can be regarded as a constant. However,

in high pressure conditions (50 MPa), the value of $\left(1-\frac{\rho_g}{\rho_a}\right)$ cannot be treated as constant any more; in fact, this value increases rapidly with an increase in temperature under such high-pressure conditions.

On the contrary, the value of $\frac{n_{ab}}{n_{max}}$ decreases sharply when the temperature increases under low pressure conditions, which is shown in the red curve in Figure 4-9-b; nevertheless, in a high pressure condition, the value of $\frac{n_{ab}}{n_{max}}$ does not change much as temperature increases. The reason behind this phenomenon is that under the effect of high pressure, the methane molecules are strongly adsorbed onto a shale surface and, therefore, the effect of temperature is less significant under such conditions. This time, the value of $\frac{n_{ab}}{n_{max}}$ is treated as a constant.

To demonstrate the effect of relative magnitudes of $\frac{n_{ab}}{n_{max}}$ and $\left(1-\frac{\rho_g}{\rho_a}\right)$ on excess adsorption, Figure 4-10 is generated showing the relationship of the multiples of these two terms with respect to temperature under both high pressure and low-pressure conditions. In this figure, the increase and decrease of the excess adsorption under these pressure and temperature conditions can be clearly observed. As one can see, under low pressure conditions, the excess adsorption decreases when the temperature increases, while, under high pressure conditions, the excess adsorption increases as the temperature increases. Thus, these distinct behaviors of excess adsorption corresponding to temperature changes explain the crossover of the excess isotherms as shown in Figure 4-8.

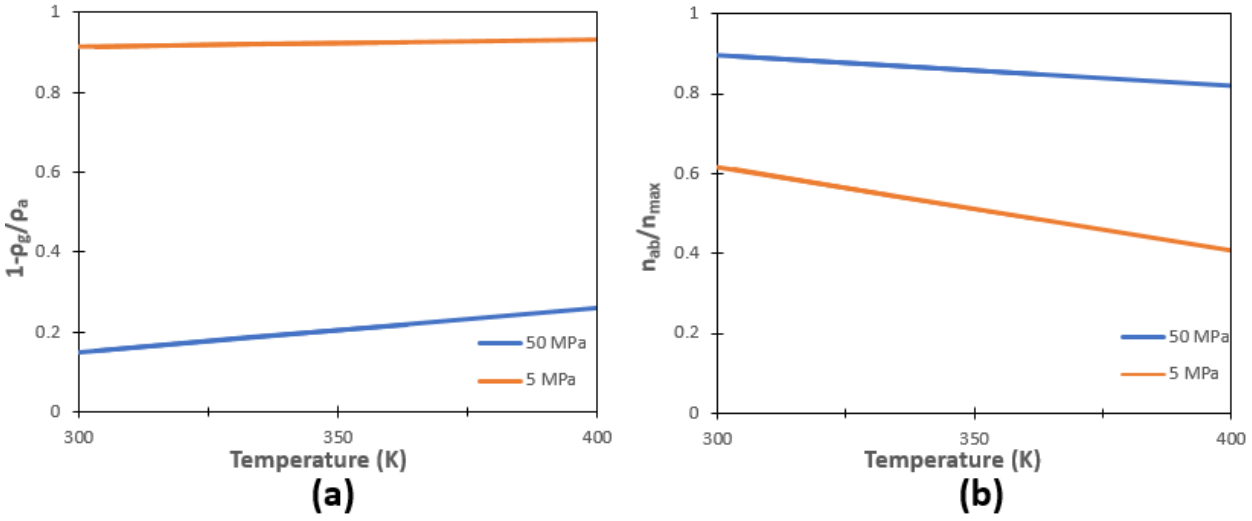

Figure 4-9. Temperature effect on the magnitude of (a) $\left(1-\frac{\rho_g}{\rho_a}\right)$ and (b) $\frac{n_{ab}}{n_{max}}$ under 5 MPa and 50 MPa (Li et al., 2018)

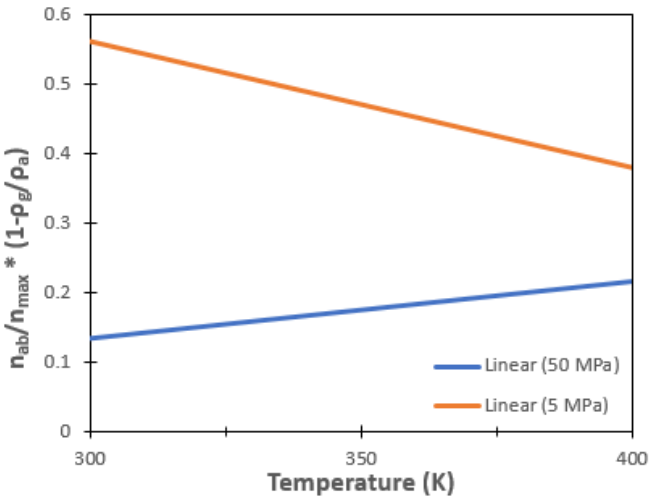

Figure 4-10. Temperature effect on the multiple of $\left(1-\frac{\rho_g}{\rho_a}\right)$ and $\frac{n_{ab}}{n_{max}}$ under 5 MPa and 50 MPa

4.4 Summary

In this chapter, four samples of shales are selected to carry out the methane adsorption analysis, and the obtained results are then used to validate the single-site and multi-site excess adsorption models proposed in the previous chapter. In summary, the following conclusions can be drawn:

- Several laboratory tests have been conducted to understand the characteristics of these shale samples. The results have shown that these samples have many features in common, such as the primary compositions of the content being quartz, clay, and type II matured kerogen. Once the physical properties of these samples are studied, a series of adsorption isotherms analyses, with a wide range of pressures and temperatures, corresponding to the actual shale reservoir condition, are then carried out for these samples.
- Both the single-site and multi-site excess adsorption models achieved satisfying fitting results with the actual measured data. Nevertheless, the multi-site model is capable of addressing the heterogeneity of shales by a wide range of adsorption energy distributions (owing to the complex compositions and different pore sizes), which is different from the single-site model only characterized by single adsorption energy. Consequently, the multi-site model results have better accuracy against the experimental data.
- Different trends of absolute adsorption and excess adsorption isotherms are observed. For the absolute adsorption isotherms, the adsorption amount always decreases with an increase in temperature. However, the crossovers are always observed in the excess adsorption isotherms. In low-pressure conditions, the excess adsorption increases as the temperature increases, but an opposite trend occurs in high-pressure conditions. The crossover depends on the relative magnitudes of $\frac{n_{ab}}{n_{max}}$ and $\left(1-\frac{\rho_g}{\rho_a}\right)$.

Chapter 5: Gas-In-Place Calculation and Analysis

5.1 Gas-In-Place Calculation Methods

In Chapter 3, we have proposed two multi-site adsorption models; one is for the absolute adsorption, and the other is for the excess adsorption. In this chapter, we will use these two derived models to calculate the total gas in place (GIP) for the shale reservoir in which the shales samples are collected. We will compare and analyze the GIP results calculated by using these two different methods and choose one that can accurately estimate the total gas in the shale reservoir.

Unlike conventional gas reservoirs, shale gas reservoirs are characterized by their plenty of nanopores that are present inside the reservoirs. Those widely existing nanopores confinement can lead to significant storage of methane that cannot be ignored when it comes to predicting the GIP for a reservoir.

The GIP calculation is generally composed of two terms; one term is the free gas (also known as the compressed gas) that occupies the reservoir void space. The state of this free gas can be characterized by the EOS equation discussed in Chapter 2. The other term is the gas that is in the adsorbed phase. Their relationship is illustrated in the following equation:

$$GIP = n_f + n_a \tag{5.1}$$

where n_f represents the amount of methane in the free gas phase and n_a represents the total amount of gas in the adsorbed phase.

An accurate estimate of GIP depends on the precise quantification of the free gas present as well as the amount of gas in the adsorbed phase. Since we have two models of adsorption available, it is then critical to understand which model to apply when calculating GIP to have an

accurate estimation of the shale gas storage capacity. The following two sub-sections will introduce each of these methods in detail.

5.1.1 Absolute adsorption method.

The absolute adsorption method for calculating the amount of methane in the adsorbed phase of the GIP equation is derived from the measured adsorption data and combines them with the absolute adsorption equation (3.5). Figure 5-1 shows how this method performs for calculating the GIP. As one can see, GIP, in this case, is calculated by merely adding the free gas in the void space and the gas in the absolute adsorbed phase. Thus, the equation for this relationship is shown as follows:

$$GIP_{ab} = n_f + n_{ab} \tag{5.2}$$

where n_{ab} is the amount of gas in absolute adsorbed phase.

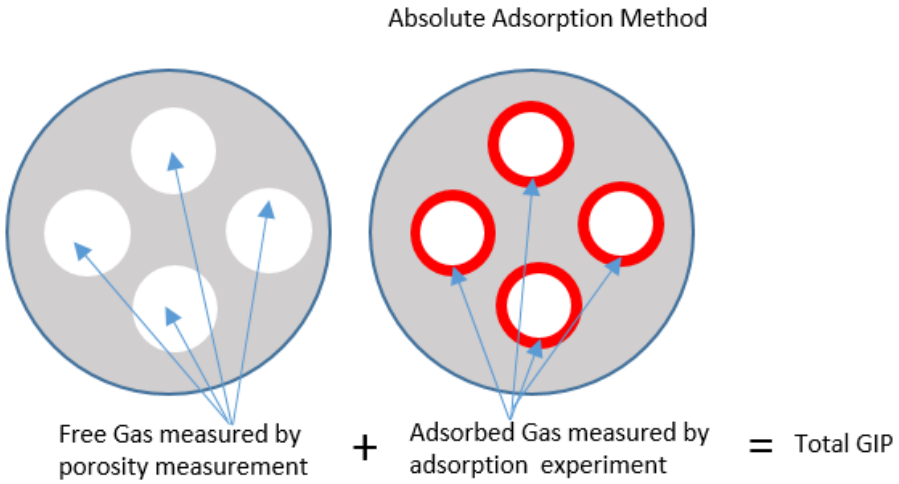

Figure 5-1. Illustration of absolute adsorption method for GIP calculation

5.1.2 Excess adsorption method.

The excess adsorption method for calculating the amount of gas in the adsorbed phase of the GIP equation is obtained from the excess adsorption equation (3.9). Figure 5-2 shows the

how this method performs for calculating the GIP. As one can see, unlike the absolute adsorption method, GIP, in this case, is calculated by adding the free gas in the void space and the gas in the absolute adsorbed phase, and is then subtracted with the free gas volume occupied by the adsorbed gas phase. According to the definition of excess adsorption in Chapter 2, the absolute adsorption minus the amount of free gas volume taken by the adsorbed gas phase equals the excess adsorption. Therefore, the equation for calculating GIP using this method is as follows:

$$GIP_{ex} = n_f + n_{ex} \tag{5.3}$$

where n_{ex} represents the total amount of gas in the excess adsorbed phase.

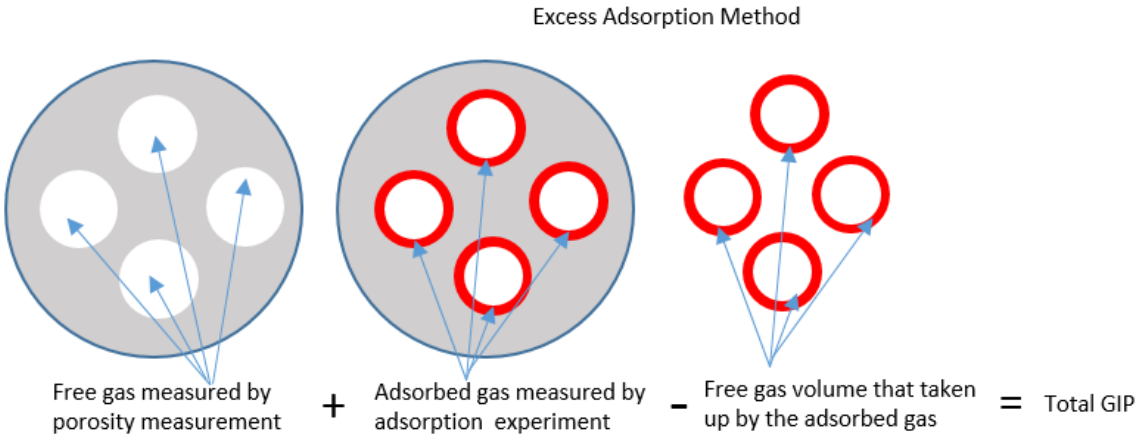

Figure 5-2. Illustration of excess adsorption method for GIP calculation

5.2 Comparison and Analysis of GIP Calculation Methods

As discussed in Chapter 2, the main difference between the absolute adsorption method and the excess adsorption method used in the GIP calculation is whether the adsorbed gas amount is quantified as the absolute adsorption uptake or excess adsorption uptake. The absolute adsorption method takes the volume of the adsorbed phase into account, while the excess adsorption method excludes the free gas volume that is occupied by the adsorbed gas phase.

Therefore, when applying these two methods in the GIP calculation, their results will be significantly different.

5.2.1 Comparison of absolute and excess adsorption uptake.

The comparisons of absolute and excess adsorption uptake concerning temperature and pressure have been made in Chapter 3. One of the conclusions we made is that the absolute adsorption always yields more substantial adsorption amount than the excess adsorption due to their differences in nature.

Now, we want to investigate the absolute adsorption and excess adsorption under the reservoir conditions. To do that, first we need to obtain the reservoir depth *H* dependent geologic temperature and pressure, shown as follows:

$$T_H = T_0 + \alpha * H \tag{5.4 a}$$

$$P_H = P_0 + \beta * H \tag{5.4 b}$$

where T_H is the temperature at a specific reservoir depth, in ^{0} C; T_0 is the surface temperature, 20 ^{0} C; α is the geothermal gradient, 2.83 ^{0} C/100 m; H is the reservoir depth, in km; P_H is the pressure at a specific reservoir depth, in MPa; P_0 is the surface pressure, 0.1 MPa; β is the pressure coefficient, 1.45 MPa/100 m.

Now that we have the reservoir temperature and pressure as a function of reservoir depth, the next step is to obtain the absolute adsorption and excess adsorption models in the reservoir conditions. For the absolute adsorption model, we substitute these two reservoir temperature and pressure equations into equation (3.5) as follows:

$$n_{ab} = n_{max} \sum_{i=1}^{i=n} \alpha_{(i)} \frac{P_0+\beta*H}{P_{L(i)}+P_0+\beta*H} \tag{5.5 a}$$

$$P_{L(i)} = P^0 \exp\left(-\frac{\Delta S^0_{(i)}}{R}\right)\exp\left(-\frac{Q_{st(i)}}{R*(T_0+\alpha*H)}\right) \quad (5.5\ b)$$

Similarly, to obtain the excess adsorption model in the reservoir conditions, we substitute these two reservoir temperature and pressure equations again into equation (3.9) as follows:

$$n_{ex} = n_{max} \sum_{i=1}^{i=n} \alpha_{(i)} \frac{P_0+\beta*H}{P_{L(i)}+P_0+\beta*H} \cdot \left(1 - \frac{\rho_g}{\rho_l} e^{\lambda((T_0+\alpha*H)-T_b)}\right) \quad (5.6\ a)$$

$$P_{L(i)} = P^0 \exp\left(-\frac{\Delta S^0_{(i)}}{R}\right)\exp\left(-\frac{Q_{st(i)}}{R*(T_0+\alpha*H)}\right) \quad (5.6\ b)$$

Once we have the absolute adsorption and excess adsorption models as a function of reservoir depth, we are ready to plot and compare the adsorption uptake of these two models concerning reservoir depth for the four shale samples, as shown in Figure 5-3. For all the samples, the excess adsorption model yields significantly less than the absolute adsorption model as the reservoir depths continues to increase. In the shallow reservoir burial depth (up to 300 m), the adsorption amounts of absolute and excess adsorption for all samples are almost identical. However, as the reservoir depth increases, the difference between absolute and excess adsorption start to become significant. This is due to an increase in pressure, which increases linearly as the reservoir depth increases.

These two trends of adsorption behaviors observed are identical to those shown in the plot of absolute adsorption and excess adsorption uptakes against the pressure. It is then clear that applying the absolute adsorption model to calculate the GIP can potentially overestimate the actual GIP as compared with using the excess adsorption model. More details utilizing these two methods of calculating GIP will be discussed and analyzed in the next sub-section.

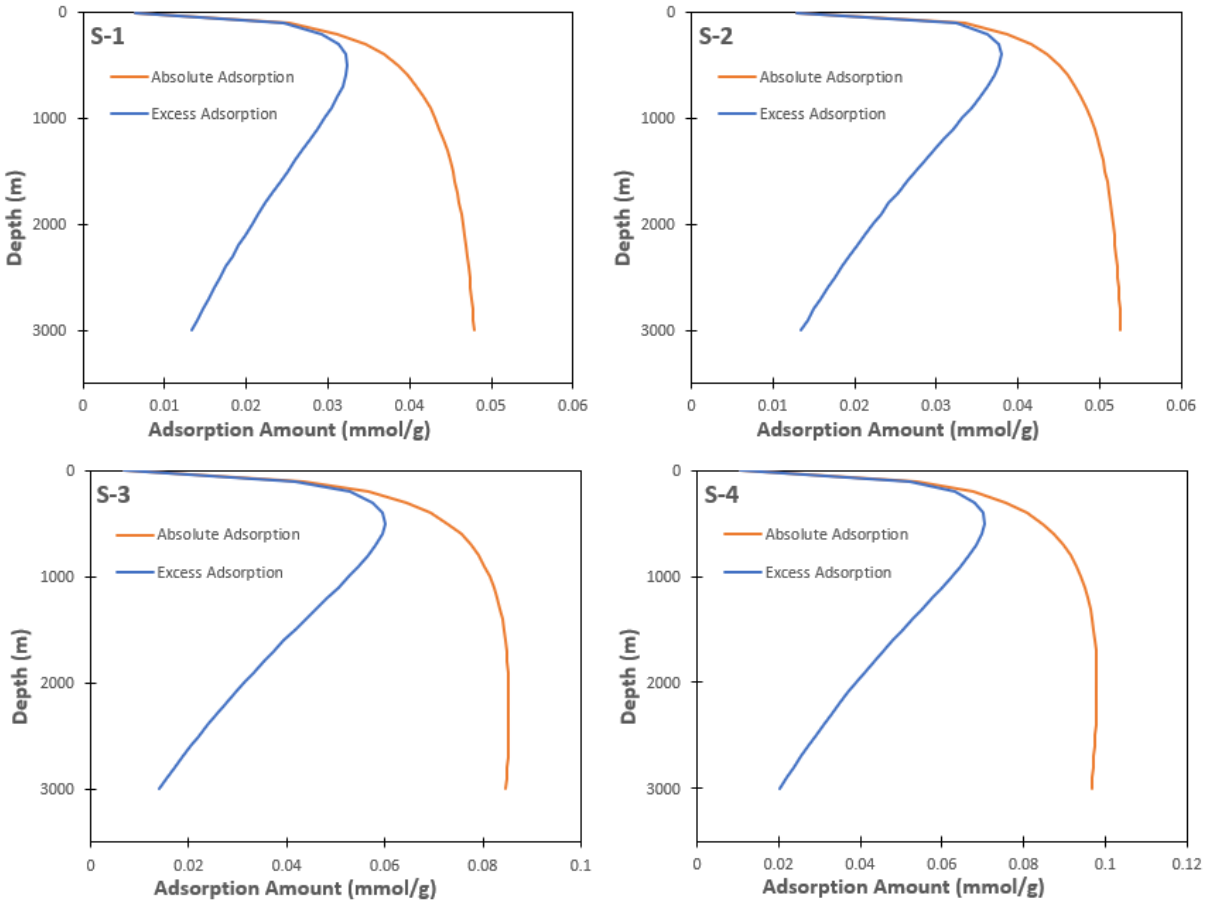

Figure 5-3. Comparison of absolute and excess adsorption concerning reservoir depth for four shale samples

5.2.2 Comparison of GIP estimation by absolute and excess methods.

Through the previous analysis, we understand the trend of adsorption behaviors of these two adsorption calculation methods in the reservoir conditions. Now, we will add the free gas amount to the adsorbed gas amount by these two methods, respectively, to compare their differences regarding the total GIP.

We modify equation (2.4 a) for the free gas density to obtain the equation for the free gas amount, as shown as follows:

$$n_f = \frac{P*V_t}{Z(P,T)*R*T} = \frac{(P_0+\beta*H)*V_t}{Z(H)*R*(T_0+\alpha*H)} \tag{5.7}$$

where V_t is the total pore space (the sum of the effective space and adsorbed phase volume).

Now, we have the equation for calculating the free gas amount, and we then add it with the adsorbed phase gas amount to obtain the GIP equation. For the absolute adsorption method, the GIP equation is as follows:

$$GIP_{ab} = n_f + n_{ab} = \frac{(P_0+\beta*H)*V_t}{Z(H)*R*(T_0+\alpha*H)} + n_{max}\sum_{i=1}^{i=n}\alpha_{(i)}\frac{P_0+\beta*H}{P_{L(i)}+P_0+\beta*H} \quad (5.8)$$

For the excess adsorption method, the GIP is calculated as follows:

$$GIP_{ex} = n_f + n_{ex} \quad (5.9)$$

$$= \frac{(P_0+\beta*H)*V_t}{Z(H)*R*(T_0+\alpha*H)} + n_{max}\sum_{i=1}^{i=n}\alpha_{(i)}\frac{P_0+\beta*H}{P_{L(i)}+P_0+\beta*H}\cdot\left(1-\frac{\rho_g}{\rho_l}e^{\lambda((T_0+\alpha*H)-T_b)}\right)$$

Once we have the above two equations, we then plot the GIP calculated by these two methods against the reservoir depth for all four samples, as shown in Figure 5-4. As one can see, the amount of GIP calculated using the excess adsorption method yields less amount compared to the results calculated using the absolute adsorption method for all the samples. This difference is due to the fact that excess adsorption does not include the free gas volume that takes up the adsorbed phase volume. Since the actual reservoir depth of our case is around 2600 m, choosing excess adsorption in GIP calculation will be more appropriate than absolute adsorption. This shows that the conventional method of applying the absolute adsorption calculation method will end up over-estimating the actual methane available in a shale reservoir and, therefore, cannot reflect the reality of the resources accurately.

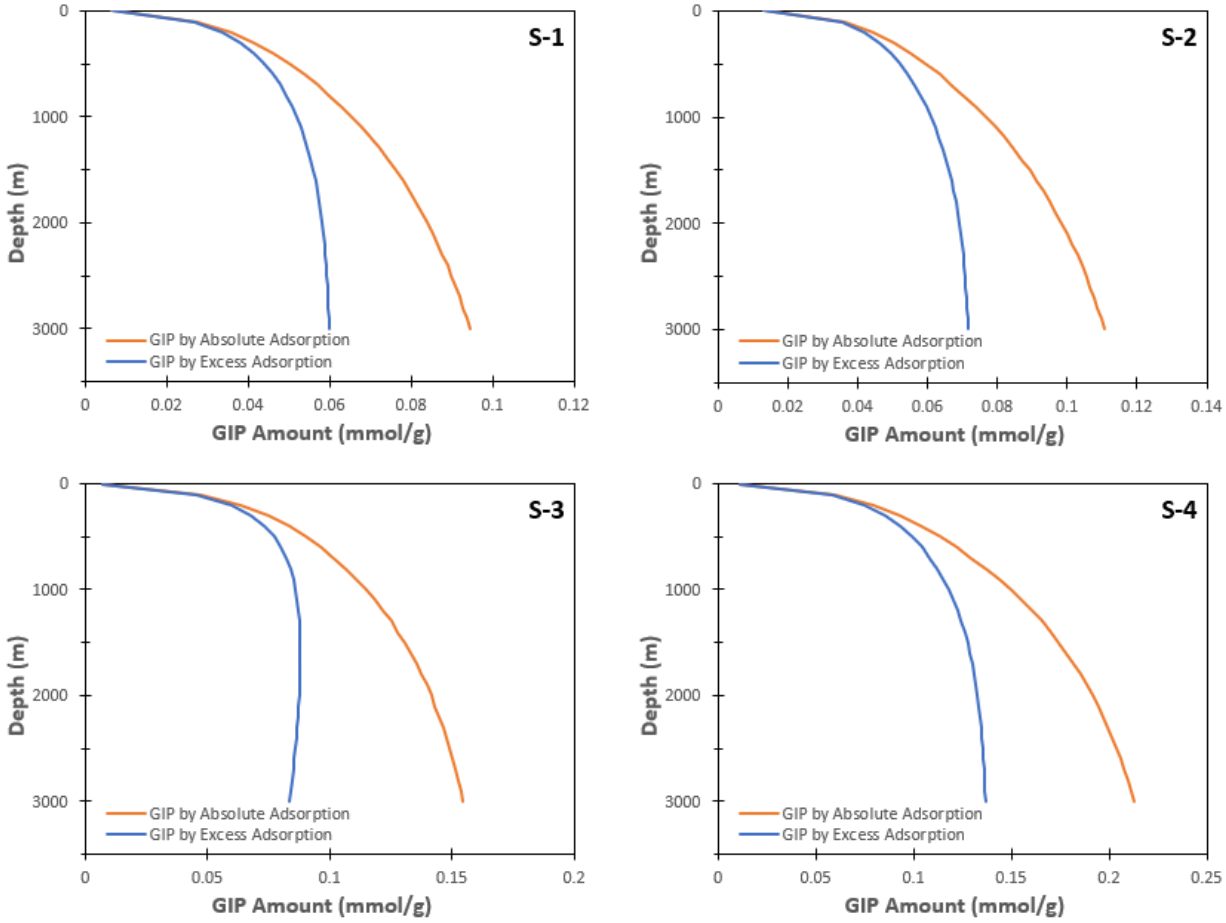

Figure 5-4. Comparison of absolute adsorption method and excess adsorption method for calculating GIP concerning reservoir depth

5.2.3 Comparison of GIP estimation by single-site and multi-site models.

From previous discussion, we have known that applying excess adsorption calculation method is more appropriate for our studied shale gas reservoir while using absolute adsorption calculation method would overestimate the actual GIP. In this sub-section, we will further compare and analyze single-site and multi-site excess adsorption GIP calculation methods.

First, we obtain the single-site excess adsorption equation concerning reservoir depth by substituting equation (5.4 a, b) into equation (3.8) as follows:

$$n_{ex(s)} = n_{max}\frac{P_0+\beta*H}{P_L+P_0+\beta*H}\cdot\left(1-\frac{\rho_g}{\rho_l}e^{\lambda((T_0+\alpha*H)-T_b)}\right) \tag{5.10}$$

Then we add the free gas equation (5.7) to equation (5.10) to generate the single-site excess adsorption GIP calculation method equation as follows:

$$GIP_{ex(s)} = n_f + n_{ex(s)} \tag{5.11}$$

$$= \frac{(P_0+\beta*H)*V_t}{Z(H)*R*(T_0+\alpha*H)} + n_{max}\frac{P_0+\beta*H}{P_L+P_0+\beta*H} \cdot \left(1 - \frac{\rho_g}{\rho_l} e^{\lambda((T_0+\alpha*H)-T_b)}\right)$$

Finally, we plot the multi-site excess adsorption GIP calculation equation (5.9) and single-site excess adsorption GIP calculation equation (5.11) together for our four samples, as shown in Figure 5-5. As one can see, the GIP results calculated by single-site and multi-site excess adsorption models are almost identical for all samples, with errors between 2% to 5%. However, the multi-site excess adsorption GIP calculation method could capture heterogeneous adsorption energy of actual shales and also achieve a more accurate adsorption amount, as it considers the heterogeneity caused by various mineral compositions and pore sizes as discussed in previous chapters. Therefore, when it comes to predicting GIP for shale gas reservoirs, a multi-site model is recommended for the excess adsorption GIP calculation method for more accurate results with consideration of gas shale heterogeneity.

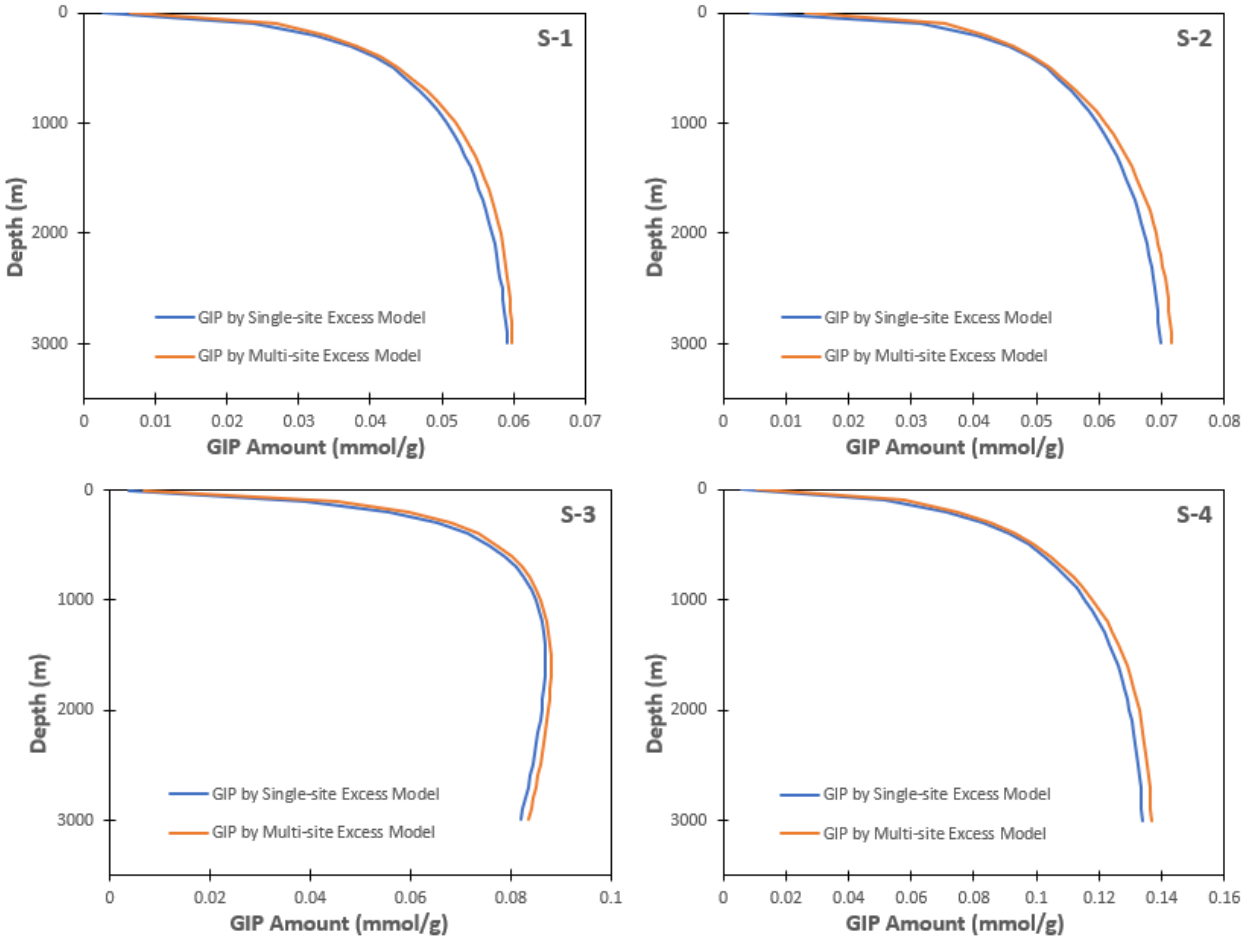

Figure 5-5. Comparison of single-site and multi-site excess adsorption GIP calculation method concerning reservoir depth

5.2.4 Comparison of adsorbed gas and free gas amount.

In this sub-section, we will compare and analyze the free gas amount and excess adsorption amount concerning reservoir depth for our four samples by using the multi-site excess adsorption GIP calculation method. A plot of free gas term and excess adsorption term from equation (5.9) is drawn for this purpose, as shown in Figure 5-6. As one can see, the amount of the adsorbed gas would gradually reach to a maximum point as the reservoir depth increases and then drops, which is consistent to the behavior of excess adsorption isotherms. However, the free gas would continue to increase as the reservoir depth increases; this is due to the fact that the free

gas in the shale gas reservoirs becomes dense as the reservoir pressure continually increases, and thus the amount of free gas would grow with the increase in the methane density.

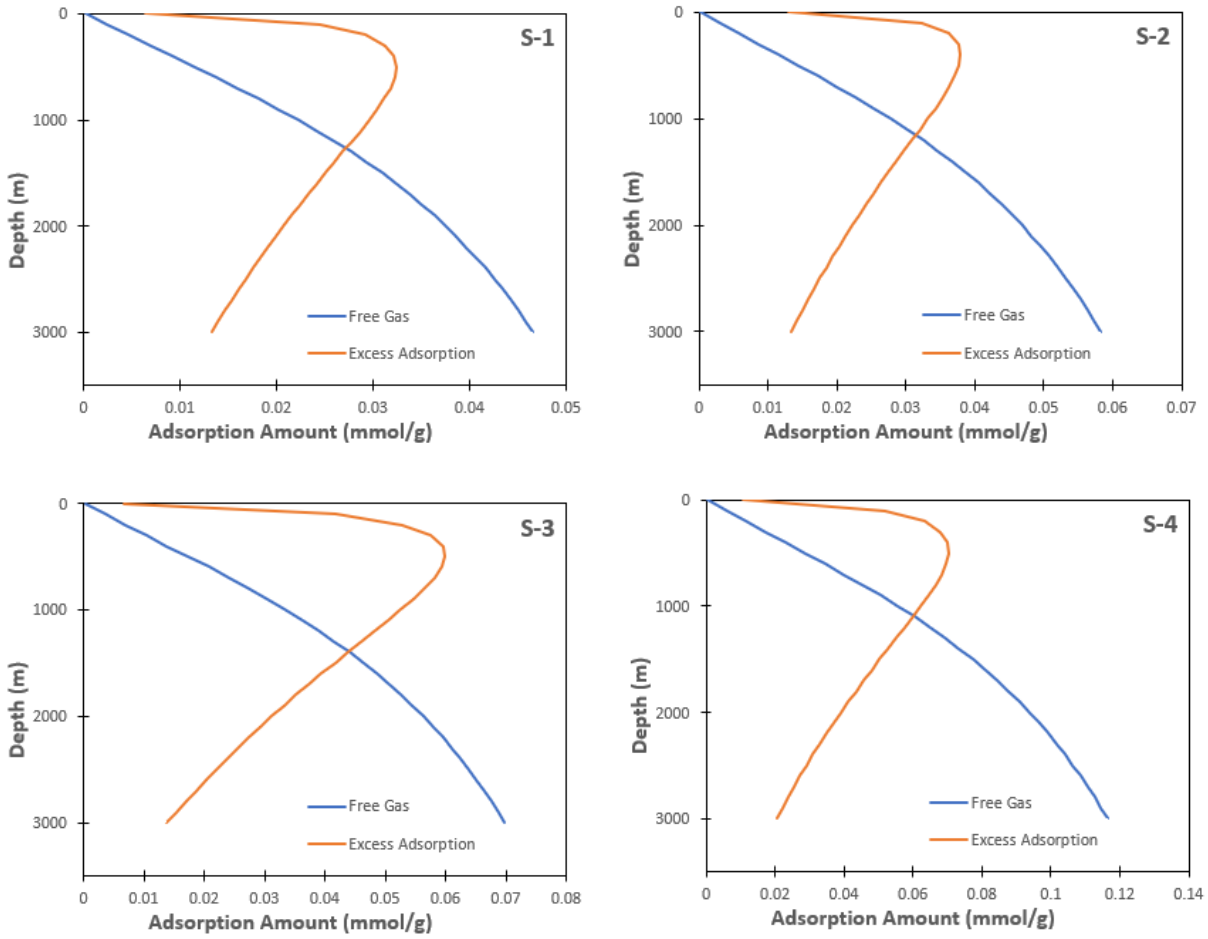

Figure 5-6. Comparison of free gas amount and excess adsorption amount concerning reservoir depth

To make it clear for the comparison between the amount of adsorbed gas and free gas, we have generated a histogram figure to illustrate the percentage of adsorbed gas and free gas with reservoir depth ranging from 100 m to 3000 m, as shown in Figure 5-7. At shallow reservoir depth, e.g., less than 1000 m, the amount of adsorbed gas is always larger than that of free gas, which is about 55% to 90% of the total GIP. However, as the reservoir depth increases, the amount of free gas would eventually exceed the amount of adsorbed gas. In our studied case, at

the reservoir depth of 2600 m, the amount of excess adsorption in the shale gas reservoir is around 30% of the GIP for our four samples.

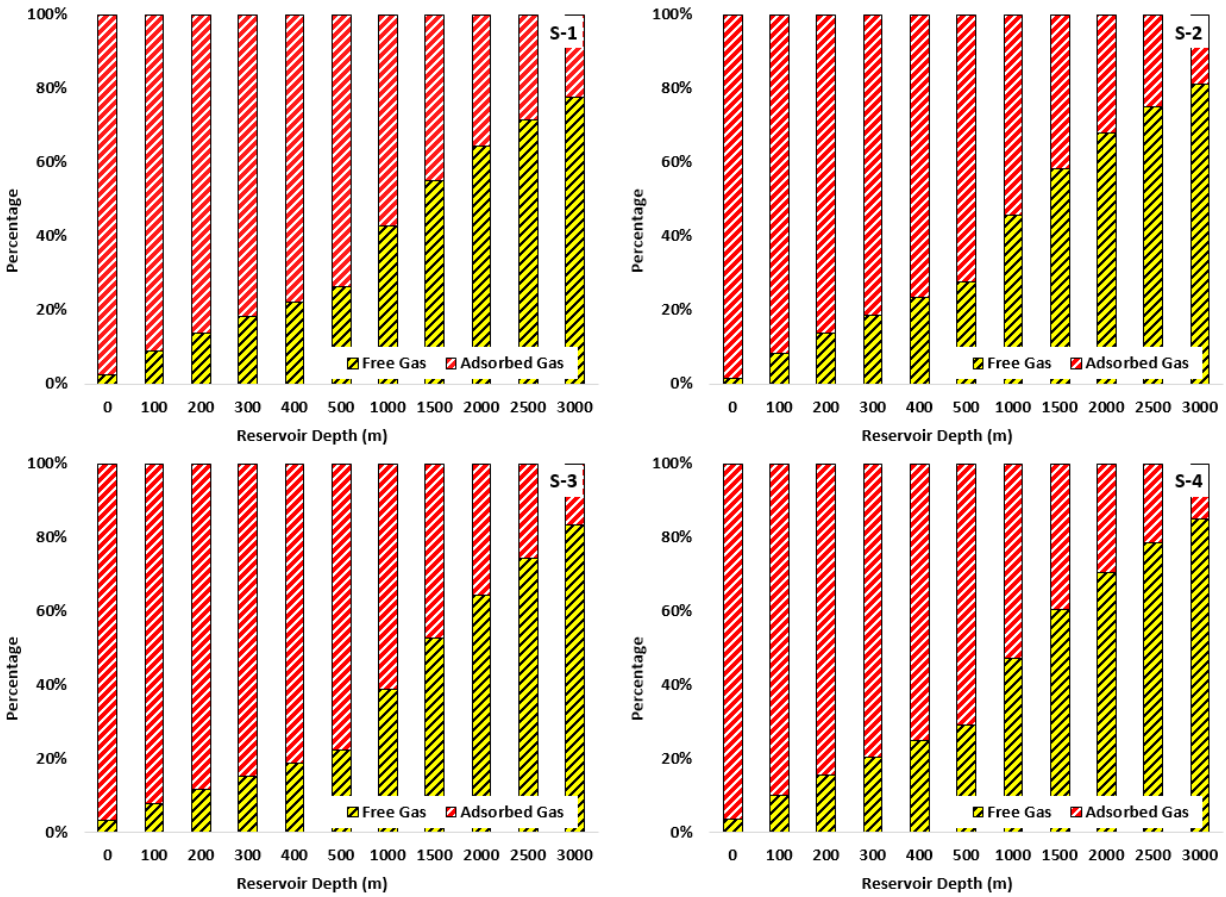

Figure 5-7. Histogram of percentage of adsorbed gas and free gas amount concerning reservoir depth

5.3 Sensitivity Analysis

Now that we already have the relationship of a GIP amount versus reservoir depth for each shale sample, the next step we would take is to analyze the parameters that affect the GIP amount. We use sample S-1 as the base case, and the parameters we investigate include the reservoir porosity, a geothermal gradient, as well as the pressure coefficient.

5.3.1 Reservoir porosity.

Figure 5-8 shows the relationship between GIP and reservoir depth when the reservoir porosity changes. As one can see in this figure, as the reservoir porosity increases from 2% to 10%, the GIP amount increases dramatically from 0.1 mmol/g to 0.47 mmol/g at 3000 m. The behavior of GIP changes indicates that the reservoir porosity is a critical parameter to consider when it comes to predicting the GIP amount. The reason is that the higher the reservoir porosity it is, the more void space there is for the free gas to occupy. Consequently, more free gas contributes to a more significant value of the GIP amount.

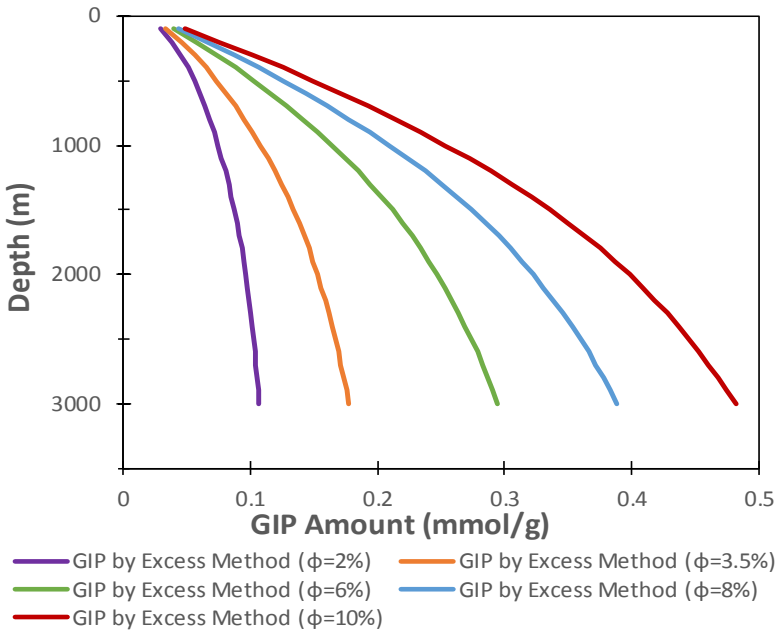

Figure 5-8. Effect of reservoir porosity on GIP calculated by excess adsorption method concerning reservoir depth

5.3.2 Temperature gradient.

Other than the parameter of the reservoir porosity, we have also analyzed the parameter related to the temperature changes in the reservoir. As Figure 5-9 shows, by increasing the geothermal gradient from 2 ^{0} C/100 m to 6 ^{0} C/100 m, while the other parameters staying the same, the GIP amount has shown a decreasing trend from 0.19 mmol/g to 0.14 mmol/g at the

3000 m depth. This behavior of the GIP amount illustrates an inverse relationship between the value of the geothermal gradient and the GIP amount.

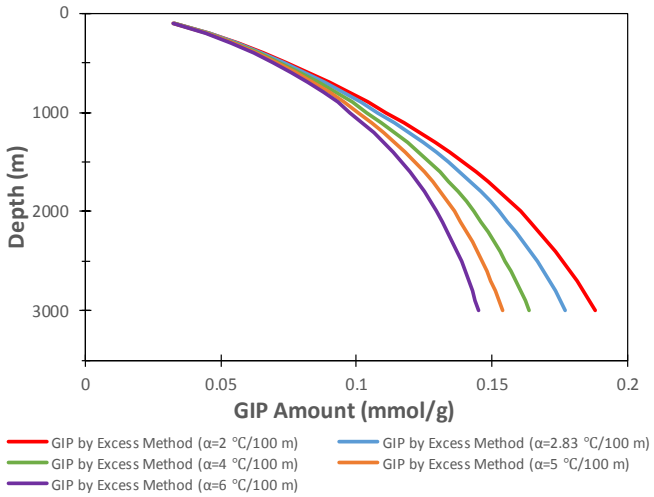

Figure 5-9. Effect of geothermal gradient on GIP calculated by excess adsorption method concerning reservoir depth

5.3.3 Pressure gradient.

To compare if the pressure coefficient has the similar effect to the geothermal gradient, we come up with Figure 5-10, with a comparison of GIP amount changes regarding the pressure coefficient varying from 1 MPa/100 m to 3 MPa/100 m while the other parameters are staying the same. As one can see in this figure, the GIP amount shows an increasing trend while the pressure coefficient increases. The value of GIP amount is 0.145 mmol/g at 3000 m when the pressure coefficient is 1 MPa/100. When the pressure coefficient changes to 3 times larger, the corresponding GIP amount increases to 0.24 mmol/g at the same reservoir depth. This behavior of the GIP amount shows that the value of a pressure gradient and the value of the GIP amount are in the same increasing trend.

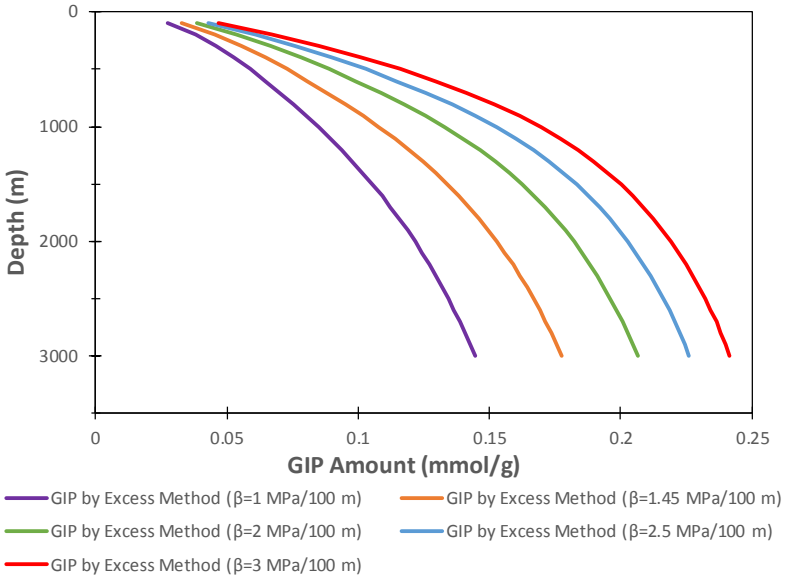

Figure 5-10. Effect of pressure coefficient on GIP calculated by excess adsorption method concerning reservoir depth

5.4 Summary

In this chapter, two methods of GIP calculations, including the absolute adsorption method and the excess adsorption method, are introduced and compared. Based on the comparison results, we are trying to illustrate the accurate method describing the actual capacity for gas storage in shale reservoirs (i.e., GIP). Also, several reservoir parameters affecting the total GIP, including the reservoir porosity, geothermal gradient, and pressure gradient are analyzed. In summary, the following conclusions can be drawn:

- The GIP for a shale reservoir is the sum of the gas amount by the adsorbed phase and the gas amount in the free phase, which is generally calculated by two methods. The GIP calculated by the conventional absolute adsorption method includes the amount of gas in the adsorbed layer and the amount of free gas in the total pore space, while the GIP calculated by the excess adsorption method excludes the volume occupied by the adsorbed molecules when calculating the free gas amount.

- In a shallow reservoir burial depth (up to 300 m), the absolute adsorption and excess adsorption are almost the same. However, as the reservoir depths increases, the absolute adsorption amount becomes more substantial than the excess adsorption one. This difference is mainly caused by an increase in pressure as the reservoir depth increases. Consequently, regarding GIP calculations, the absolute adsorption method always over-estimate sthe actual GIP in an actual shale reservoir depth (2000-3000 m).
- The GIP is affected by several parameters of reservoir properties, such as the reservoir porosity, geothermal gradient, as well as the pressure gradient. In high porosity shale gas reservoirs, the amount of free gas becomes significant, which leads to a higher GIP. As the geothermal gradient increases, an opposite trend of the GIP amount regarding the reservoir depth is observed; on the contrary, as the pressure gradient increase, a positive trend of the GIP amount regarding the reservoir depth is obtained.

Chapter 6: Conclusions and Recommendations

In this thesis, we have compared the differences between absolute adsorption and excess adsorption. For each type of these two adsorptions, we have derived single-site as well as multi-site models to describe their adsorption behaviors. In addition, we have also conducted adsorption experiments and obtained experimental data to verify these derived adsorption models. Furthermore, we have applied these adsorption models to calculate the total GIP for a shale gas reservoir. In summary, the following conclusions and future recommendations can be drawn in the following two subsections.

6.1 Conclusions

- Absolute adsorption is defined as the total amount of gas in an adsorbed layer, always described by a Langmuir equation for supercritical methane adsorption on shale, while the excess adsorption refers to the gas amount of absolute adsorption excluding the free gas amount in an adsorbed layer, which can be characterized by a Langmuir-Gibbs model. However, due to the shortcoming of an experiment method itself, the measured adsorption data is always in accordance with the excess adsorption rather than the absolute one.
- The commonly used Langmuir-based adsorption models, including the Langmuir equation and Langmuir-Gibbs equation, are based on the assumption of homogeneous adsorbent surfaces. In reality, natural shale is characterized by strong energetic heterogeneity for its wide range in pore sizes and variety of mineral compositions, which makes the homogeneous surface assumption invalid. To overcome this challenge, a multi-site model integrating the energetic heterogeneity in adsorption is derived.

- A series of adsorption isotherm experiments have been carried out over a wide range of pressures and temperatures, and the excess adsorption models, including the traditional Langmuir-Gibbs equation and a proposed multi-site one, are used to fit the measured data. After comparison, the multi-site one achieves better fitting results than the traditional one, which is attributed to its ability reflecting the heterogeneity of shales with a complex distribution in adsorption energy.
- Absolute adsorption and excess adsorption isotherms are plotted using the parameters obtained from the obtained fitting scenarios. Different trends for these two curves can be observed: a monotonic increasing trend exists in the absolute adsorption isotherm with an increase in pressure; however, for an excess adsorption one, a maximum always presents at some critical pressure. Also, these two isotherms are almost identical in low-pressure ranges, while their difference becomes evident with an increase in pressure.
- GIP is the sum of the amount of gas in both the free phase and the adsorbed phase. The free gas amount can be directly obtained by an equation of gas state (EOS) at specific pressure and temperature with respect to reservoir depth. However, the adsorbed gas amount can be quantified by both the absolute adsorption equation as well as the excess adsorption equation. It should be noted that the GIP calculated by the excess adsorption method is an accurate one, for its exclusion of the additional free gas amount in the adsorbed phase volume.
- When comparing the absolute and excess adsorption methods for calculations of the GIP, the total gas amount calculated by an absolute adsorption method (GIP_{ab}) is identical to that by an excess adsorption method (GIP_{ex}) in shallow reservoir burial depth. However, the GIP_{ab} eventually exceeds the GIP_{ex} substantially due to the increasing difference

between the absolute adsorption amount and the excess one at a high pressure condition. Therefore, the absolute adsorption method makes GIP inevitably overestimated.

- A sensitivity analysis is conducted on several reservoir properties to find out their effect on GIP, including the reservoir porosity, geothermal gradient, as well as the pressure gradient. Higher porosity leads to a greater GIP due to more void spaces for free gas to reside. As the geothermal gradient increases, the GIP becomes less at the same reservoir depth; in contrast, as the pressure gradient increases, a higher value of GIP is observed at the same reservoir depth.

6.2 Future Recommendations

- The adsorbed phase density is identified as an essential parameter for quantifying excess adsorption in our proposed excess adsorption model. However, this value is difficult to be directly measured, and it significantly depends on which method is applied. in this thesis, we employed a temperature-dependent method proposed by Ozawa et al. (1976); in the future, molecular simulation works will be conducted to obtain a more accurate estimation of this value.
- Although the multi-site adsorption model can address the energetic heterogeneity for methane adsorption on shale, the energy distribution in our proposed model is assumed as a Gauss function, because the actual energy distribution is also difficult to be directly measured. This distribution of energy might not reflect the reality of natural shale, but it is a most common assumption. Therefore, a precise methodology is needed in the future to address this complex problem.

- In our investigation of GIP calculations for shale reservoirs, both the absolute adsorption method and the excess adsorption method are applied and compared. It is found that GIP calculated by the absolute adsorption method is always larger than that calculated by the excess one, and their distinction becomes more significant in reservoirs with deep depth. Considering that the excess adsorption method can obtain an accurate GIP, therefore, it is recommended for the estimation of GIP.

References

Aguilera, R. (2014). Flow units: From conventional to tight-gas to shale-gas to tight-oil to shale-oil reservoirs. SPE Reservoir Evaluation & Engineering, 17(02), 190-208.

Ambrose, R. J., Hartman, R. C., Diaz-Campos, M., Akkutlu, I. Y., & Sondergeld, C. H. (2012). Shale Gas-in-Place Calculations Part I: New Pore-Scale Considerations. SPE Journal, 17(01), 219-229.

Bennett, K. C., Berla, L. A., Nix, W. D., & Borja, R. I. (2015). Instrumented nanoindentation and 3D mechanistic modeling of a shale at multiple scales. Acta Geotechnica, 10(1), 1-14.

Blanco, A. A. G., Vallone, A. F., Korili, S. A., Gil, A., & Sapag, K. (2016). A comparative study of several microporous materials to store methane by adsorption. Microporous and Mesoporous Materials, 224, 323-331.

Charoensuppanimit, P., Mohammad, S. A., Robinson, R. L., & Gasem, K. A. (2015). Modeling the temperature dependence of supercritical gas adsorption on activated carbons, coals and shales. International Journal of Coal Geology, 138, 113-126.

Curtis, J. B. (2002). Fractured shale-gas systems. AAPG bulletin, 86(11), 1921-1938.

Do, D. D. (1998). Adsorption analysis: equilibria and kinetics (Vol. 2, pp. 1-18). London: Imperial college press.

Do, D. D., Do, H. D., Fan, C., & Nicholson, D. (2010). On the existence of negative excess isotherms for argon adsorption on graphite surfaces and in graphitic pores under supercritical conditions at pressures up to 10,000 atm. Langmuir, 26(7), 4796-4806.

Dong, Z., Holditch, S., & McVay, D. (2013). Resource evaluation for shale gas reservoirs. SPE Economics & Management, 5(01), 5-16.

Donohue, M. D., & Aranovich, G. L. (1998). Classification of Gibbs adsorption isotherms. Advances in Colloid and Interface Science, 76, 137-152.

Dubinin, M. (1960). The potential theory of adsorption of gases and vapors for adsorbents with energetically nonuniform surfaces. Chemical Reviews, 60(2), 235-241.

Gasparik, M., Bertier, P., Gensterblum, Y., Ghanizadeh, A., Krooss, B. M., & Littke, R. (2014). Geological controls on the methane storage capacity in organic-rich shales. International Journal of Coal Geology, 123, 34-51.

Gasparik, M., Ghanizadeh, A., Bertier, P., Gensterblum, Y., Bouw, S., & Krooss, B. M. (2012). High-pressure methane sorption isotherms of black shales from the Netherlands. Energy & fuels, 26(8), 4995-5004.

Gibbs J W. The collected work of JW Gibbs [J]. Vol. I, 1931: 54-371.

Guo, C., Wei, M., & Liu, H. (2015). Modeling of Gas Production from Shale Reservoirs Considering Multiple Transport Mechanisms. Plos One, 10(12).

Hu, Y., Devegowda, D., Striolo, A., Phan, A., Ho, T. A., Civan, F., & Sigal, R. F. (2014). Microscopic dynamics of water and hydrocarbon in shale-kerogen pores of potentially mixed wettability. Spe Journal, 20(01), 112-124.

Hu, H., Zhang, T., Wiggins-Camacho, J. D., Ellis, G. S., Lewan, M. D., & Zhang, X. (2015). Experimental investigation of changes in methane adsorption of bitumen-free Woodford Shale with thermal maturation induced by hydrous pyrolysis. Marine and Petroleum Geology, 59, 114-128.

Huang, L., Ning, Z., Wang, Q., Qi, R., Zeng, Y., Qin, H., ... & Zhang, W. (2018). Molecular simulation of adsorption behaviors of methane, carbon dioxide and their mixtures on kerogen: effect of kerogen maturity and moisture content. Fuel, 211, 159-172.

International Energy Agency (IEA), 2015. World Energy Outlook 2015. IEA/OECD, Paris.www.iea.org.

Jacob, H. (1989). Classification, structure, genesis and practical importance of natural solid oil bitumen ("migrabitumen"). International Journal of Coal Geology, 11(1), 65-79.

Ji, L., Zhang, T., Milliken, K. L., Qu, J., & Zhang, X. (2012). Experimental investigation of main controls to methane adsorption in clay-rich rocks. Applied Geochemistry, 27(12), 2533-2545.

Ju, Y., Wang, G., Bu, H., Li, Q., & Yan, Z. (2014). China organic-rich shale geologic features and special shale gas production issues. Journal of Rock Mechanics and Geotechnical Engineering, 6(3), 196-207.

Knox, D., & Dadyburjor, D. B. (1981). Bounds for acceptable values of adsorption entropy. Chemical Engineering Communications, 11(1-3), 99-112.

Langmuir, I. (1918). The adsorption of gases on plane surfaces of glass, mica and platinum. Journal of the American Chemical society, 40(9), 1361-1403.

Liu, Y., Li, H. A., Tian, Y., Jin, Z., & Deng, H. (2018). Determination of the absolute adsorption/desorption isotherms of CH 4 and n-C 4 H 10 on shale from a nano-scale perspective. Fuel, 218, 67-77.

Loucks, R. G., Reed, R. M., Ruppel, S. C., & Hammes, U. (2010). Preliminary classification of matrix pores in mudrocks: Gulf Coast Association of Geological Societies Transactions, v. 60, 435-441.

Li, J., Chen, Z., Wu, K., Wang, K., Luo, J., Feng, D., ... & Li, X. (2018). A multi-site model to determine supercritical methane adsorption in energetically heterogeneous shales. Chemical Engineering Journal, 349, 438-455.

Li, J., Li, X., Wang, X., Li, Y., Wu, K., Shi, J., ... & Yu, P. (2016). Water distribution characteristic and effect on methane adsorption capacity in shale clay. International Journal of Coal Geology, 159, 135-154.

Lu, X. C., Li, F. C., & Watson, A. T. (1995). Adsorption measurements in Devonian shales. Fuel, 74(4), 599-603.

Mehta, S. D., & Danner, R. P. (1985). An improved potential theory method for predicting gas-mixture adsorption equilibria. Industrial & engineering chemistry fundamentals, 24(3), 325-330.

Mosher, K., He, J., Liu, Y., Rupp, E., & Wilcox, J. (2013). Molecular simulation of methane adsorption in micro-and mesoporous carbons with applications to coal and gas shale systems. International Journal of Coal Geology, 109, 36-44.

Murata, K., El-Merraoui, M., & Kaneko, K. (2001). A new determination method of absolute adsorption isotherm of supercritical gases under high pressure with a special relevance to density-functional theory study. The Journal of Chemical Physics, 114(9), 4196-4205.

Myers, A. L. (2002). Thermodynamics of adsorption in porous materials. AIChE Journal, 48(1), 145-160.

Nelson, P. H. (2009). Pore-throat sizes in sandstones, tight sandstones, and shales. AAPG bulletin, 93(3), 329-340.

Nikolaev, K. M., & Dubinin, M. M. (1958). Concerning adsorptional properties of carbon adsorbents 3. A study of adsorption isotherms of gases and vapors on active carbons over a wide interval of temperatures, including the critical region. Russian Chemical Bulletin, 7(10), 1124-1133.

Outlook for natural gas (2017). World Energy Outlook 2017, 333-365.

Outlook for unconventional gas (2015). World Energy Outlook 2015, 229-268.

Ozawa, S., Kusumi, S., & Ogino, Y. (1976). Physical adsorption of gases at high pressure. IV. An improvement of the Dubinin—Astakhov adsorption equation. Journal of Colloid and Interface Science, 56(1), 83-91.

Redlich, O., & Kwong, J. N. (1949). On the thermodynamics of solutions. V. An equation of state. Fugacities of gaseous solutions. Chemical reviews, 44(1), 233-244.

Reich, R., Ziegler, W. T., & Rogers, K. A. (1980). Adsorption of methane, ethane, and ethylene gases and their binary and ternary mixtures and carbon dioxide on activated carbon at 212-301 K and pressures to 35 atmospheres. Industrial & Engineering Chemistry Process Design and Development, 19(3), 336-344.

Rexer, T. F., Mathia, E. J., Aplin, A. C., & Thomas, K. M. (2014). High-pressure methane adsorption and characterization of pores in Posidonia shales and isolated kerogens. Energy & Fuels, 28(5), 2886-2901.

Roque-Malherbe, R. M. (2018). Adsorption and diffusion in nanoporous materials. Boca Raton: CRC Press/Taylor & Francis.

Ross, D. J., & Bustin, R. M. (2009). The importance of shale composition and pore structure upon gas storage potential of shale gas reservoirs. Marine and Petroleum Geology, 26(6), 916-927.

Saha, D., Grappe, H. A., Chakraborty, A., & Orkoulas, G. (2016). Postextraction Separation, On-Board Storage, and Catalytic Conversion of Methane in Natural Gas: A Review. Chemical Reviews, 116(19), 11436-11499.

Sayed, M. A., Al-Muntasheri, G. A., & Liang, F. (2017). Development of shale reservoirs: Knowledge gained from developments in North America. Journal of Petroleum Science and Engineering, 157, 164-186.

Setzmann, U., & Wagner, W. (1991). A new equation of state and tables of thermodynamic properties for methane covering the range from the melting line to 625 K at pressures up to 100 MPa. Journal of Physical and Chemical Reference Data, 20(6), 1061-1155.

Shabani, M., Moallemi, S. A., Krooss, B. M., Amann-Hildenbrand, A., Zamani-Pozveh, Z., Ghalavand, H., & Littke, R. (2018). Methane sorption and storage characteristics of organic-rich carbonaceous rocks, Lurestan province, southwest Iran. International Journal of Coal Geology, 186, 51-64.

Tang, X., Ripepi, N., Stadie, N. P., Yu, L., & Hall, M. R. (2016). A dual-site Langmuir equation for accurate estimation of high pressure deep shale gas resources. Fuel, 185, 10-17.

Tian, Y., Yan, C., & Jin, Z. (2017). Characterization of methane excess and absolute adsorption in various clay nanopores from molecular simulation. Scientific Reports, 7(1), 12040.

Wood, D. A., & Hazra, B. (2017). Characterization of organic-rich shales for petroleum exploration & exploitation: A review-Part 3: Applied geomechanics, petrophysics and reservoir modeling. Journal of Earth Science, 28(5), 779-803.

Wu, K., Chen, Z., Li, X., & Dong, X. (2016). Methane storage in nanoporous material at supercritical temperature over a wide range of pressures. Scientific Reports, 6, 33461.

Xia, X., Litvinov, S., & Muhler, M. (2006). Consistent approach to adsorption thermodynamics on heterogeneous surfaces using different empirical energy distribution models. Langmuir, 22(19), 8063-8070.

Xia, X., d'Alnoncourt, R. N., & Muhler, M. (2008). Entropy of adsorption of carbon monoxide on energetically heterogeneous surfaces. Journal of Thermal Analysis and Calorimetry, 91(1), 167-172.

Xiong, J., Liu, X., Liang, L., & Zeng, Q. (2017). Adsorption of methane in organic-rich shale nanopores: An experimental and molecular simulation study. Fuel, 200, 299-315.

Yang, F., Ning, Z., Zhang, R., Zhao, H., & Krooss, B. M. (2015). Investigations on the methane sorption capacity of marine shales from Sichuan Basin, China. International Journal of Coal Geology, 146, 104-117.

Yang, F., Xie, C., Xu, S., Ning, Z., & Krooss, B. M. (2017). Supercritical methane sorption on organic-rich shales over a wide temperature range. Energy & Fuels, 31(12), 13427-13438.

Zhiltsov, S. S., & Zonn, I. S. (2016). The Evaluation of the World Potential of Shale Gas Reserves. The Handbook of Environmental Chemistry Shale Gas: Ecology, Politics, Economy, 17-24.

Zhang, J., Clennell, M. B., Liu, K., Pervukhina, M., Chen, G., & Dewhurst, D. N. (2016). Methane and carbon dioxide adsorption on Illite. Energy & Fuels, 30(12), 10643-10652.

Zhang, T., Ellis, G. S., Ruppel, S. C., Milliken, K., & Yang, R. (2012). Effect of organic-matter type and thermal maturity on methane adsorption in shale-gas systems. Organic geochemistry, 47, 120-131.

Zhu, X., & Zhao, Y. P. (2014). Atomic mechanisms and equation of state of methane adsorption in carbon nanopores. The Journal of Physical Chemistry C, 118(31), 17737-17744.